

1 **Structural basis for broad sarbecovirus neutralization by a human monoclonal antibody**

2
3 M. Alejandra Tortorici^{1,2,*}, Nadine Czudnochowski^{3,*}, Tyler N. Starr^{4,*}, Roberta Marzi^{5,*},
4 Alexandra C. Walls¹, Fabrizia Zatta⁵, John E. Bowen¹, Stefano Jaconi⁵, Julia di iulio³, Zhaoqian
5 Wang¹, Anna De Marco⁵, Samantha K. Zepeda¹, Dora Pinto⁵, Zhuoming Liu⁶, Martina
6 Beltramello⁵, Istvan Bartha⁵, Michael P. Housley³, Florian A. Lempp³, Laura E. Rosen³, Exequiel
7 Dellota Jr.³, Hannah Kaiser³, Martin Montiel-Ruiz³, Jiayi Zhou³, Amin Addetia⁴, Barbara
8 Guarino³, Katja Culap⁵, Nicole Sprugasci⁵, Christian Saliba⁵, Eneida Vetti⁵, Isabella Giacchetto-
9 Sasselli⁵, Chiara Silacci Fregni⁵, Rana Abdelnabi⁷, Shi-Yan Caroline Foo⁷, Colin Havenar-
10 Daughton³, Michael A. Schmid⁵, Fabio Benigni⁵, Elisabetta Cameroni⁵, Johan Neyts⁷, Amalio
11 Telenti³, Gyorgy Snell³, Herbert W. Virgin³, Sean P.J. Whelan⁶, Jesse D. Bloom^{4,8}, Davide Corti^{5,#},
12 David Veessler^{1,#} & Matteo Samuele Pizzuto^{5,#}

13
14 ¹Department of Biochemistry, University of Washington, Seattle, Washington 98195, USA.

15 ²Institut Pasteur and CNRS UMR 3569, Unité de Virologie Structurale, Paris, France

16 ³Vir Biotechnology, San Francisco, CA 94158, USA.

17 ⁴Basic Sciences Division and Computational Biology Program, Fred Hutchinson Cancer
18 Research Center, Seattle, WA 98109, USA.

19 ⁵Humabs Biomed SA, a subsidiary of Vir Biotechnology, 6500 Bellinzona, Switzerland.

20 ⁶Department of Molecular Microbiology, Washington University School of Medicine, St. Louis,
21 MO, 63110, USA.

22 ⁷Rega Institute for Medical Research, Laboratory of Virology and Chemotherapy, KU Leuven,
23 Belgium.

24 ⁸Howard Hughes Medical Institute, Seattle, WA 98109, USA.

25
26 *These authors contributed equally

27
28 #Correspondence: mpizzuto@vir.bio, dveessler@uw.edu, dcorti@vir.bio

29
30
31
32
33
34
35
36
37
38
39
40

41 **The recent emergence of SARS-CoV-2 variants of concern (VOC) and the recurrent**
42 **spillovers of coronaviruses in the human population highlight the need for broadly**
43 **neutralizing antibodies that are not affected by the ongoing antigenic drift and that can**
44 **prevent or treat future zoonotic infections. Here, we describe a human monoclonal antibody**
45 **(mAb), designated S2X259, recognizing a highly conserved cryptic receptor-binding domain**
46 **(RBD) epitope and cross-reacting with spikes from all sarbecovirus clades. S2X259 broadly**
47 **neutralizes spike-mediated entry of SARS-CoV-2 including the B.1.1.7, B.1.351, P.1 and**
48 **B.1.427/B.1.429 VOC, as well as a wide spectrum of human and zoonotic sarbecoviruses**
49 **through inhibition of ACE2 binding to the RBD. Furthermore, deep-mutational scanning**
50 **and *in vitro* escape selection experiments demonstrate that S2X259 possesses a remarkably**
51 **high barrier to the emergence of resistance mutants. We show that prophylactic**
52 **administration of S2X259 protects Syrian hamsters against challenges with the prototypic**
53 **SARS-CoV-2 and the B.1.351 variant, suggesting this mAb is a promising candidate for the**
54 **prevention and treatment of emergent VOC and zoonotic infections. Our data unveil a key**
55 **antigenic site targeted by broadly-neutralizing antibodies and will guide the design of pan-**
56 **sarbecovirus vaccines.**

57
58
59
60
61
62
63
64
65
66
67
68
69
70
71
72
73
74
75
76
77
78
79

80 Zoonotic pathogens are mainly responsible for dead-end infections but can be stably
81 introduced in the new host sporadically as a result of adaptive mutations. Two coronaviruses
82 (SARS-CoV and SARS-CoV-2) from distinct clades within the sarbecovirus subgenus have
83 jumped from their natural hosts to humans in the last 20 years, with sustained person-to-person
84 transmission^{1, 2}. In contrast to SARS-CoV, which was brought under control in 2003 and
85 disappeared in 2004 after claiming 774 lives, the emergence of SARS-CoV-2 at the end of 2019
86 has resulted in a global pandemic causing over 132 million infections and more than 2.8 million
87 fatalities as of April 2021. SARS-CoV-2 genetic drift has resulted in new emerging variants of
88 concern (VOC) characterized by higher transmissibility, immune evasion and/or disease severity
89 such as B.1.1.7, B.1.351, B.1.429, and P.1 originally identified in the UK, South Africa, California,
90 and Brazil, respectively³⁻⁶. Furthermore, recent data suggest that people infected with or vaccinated
91 against the prototypic SARS-CoV-2 virus may have reduced protection from reinfection with these
92 variants⁷⁻¹⁵. Therefore, pan-sarbecovirus countermeasures, such as vaccines and therapeutics, are
93 needed to cope with SARS-CoV-2 evolution and to protect against future sarbecovirus emergence.

94 Similar to other coronaviruses, the sarbecovirus spike protein (S) mediates viral entry into
95 host cells, represents the main target of neutralizing antibodies (nAbs) and is the focus of vaccine
96 design. S comprises an S₁ subunit, which recognizes host cell receptors, and an S₂ subunit that
97 promotes viral-cell membrane fusion^{16, 17}. The S₁ subunit includes the receptor-binding domain
98 (RBD, also called S1^B), which in the case of SARS-CoV and SARS-CoV-2 interacts with
99 angiotensin-converting enzyme 2 (ACE2) to allow the virus to enter cells^{1, 16, 18-20}.

100 A highly conserved region on the sarbecovirus RBDs, designated antigenic site II²¹, has
101 been shown to elicit SARS-CoV and SARS-CoV-2 cross-neutralizing Abs (also defined as class 4
102 RBD-specific Abs)^{22, 23}. However, site II is cryptic and becomes accessible only when at least two
103 RBDs in the spike trimer adopt an open conformation and thus it is poorly immunogenic, as
104 demonstrated by the low percentage of antibodies targeting this site in SARS-CoV-2 exposed
105 individuals^{21, 23}. Here we describe a site II-targeting mAb designated S2X259, which was isolated
106 from an infected SARS-CoV-2-exposed subject, that possesses exceptional neutralization breadth
107 within the sarbecovirus subgenus, including all VOC, and remarkable resistance to escape
108 mutations. In addition, we show that S2X259 neutralizes ACE2-dependent SARS-CoV and SARS-
109 CoV-2 related pseudoviruses with multiple mechanisms of action and that prophylactic
110 administration of this mAb protects Syrian hamsters against SARS-CoV-2 challenge, including
111 with the B.1.351 VOC. Overall, our findings indicate that S2X259 is a promising countermeasure
112 to simultaneously protect against SARS-CoV-2 antigenic drift as well as emerging zoonotic
113 sarbecoviruses and highlight the importance of RBD site II for pan-sarbecovirus vaccine design.

114

115

116 **Identification of a broadly neutralizing sarbecovirus mAb**

117 To identify mAbs with potent and broad neutralizing activity against sarbecoviruses, we
118 sorted SARS-CoV-2 S-specific (IgG) memory B cells from one COVID-19 convalescent

119 individual 75 days after symptoms onset. We identified one mAb, designated S2X259, derived
120 from VH1-69/D3-10/JH3 and VL1-40/JH3 genes (VH and VL 94.1% and 98.26 % identical to V
121 germline genes, respectively) (**Table S1**), which cross-reacted with 29 out of 30 S glycoproteins
122 representative of all sarbecovirus clades^{22,24} and current SARS-CoV-2 VOCs transiently expressed
123 in ExpiCHO cells (**Fig. 1a,b**). The recognition of spikes from the divergent bat Asian-related
124 (clade 2) and bat non-Asian (clade 3) clades highlights the exceptional breadth of this mAb (**Fig.**
125 **1a,b**).

126 The cross-reactivity of S2X259 within the sarbecovirus subgenus was further confirmed
127 using ELISA with a panel of 12 RBDs (**Fig. 1c**). S2X259 bound tightly to all RBDs tested (EC50
128 < 30 ng/ml) with the exception of two bat strains ZC45 (EC50 = 539 ng/ml) and Anlong-
129 112 (EC50 = 1281 ng/ml) (**Fig. 1c**). Surface plasmon resonance (SPR) indicated that the S2X259
130 Fab fragment bound to clade 1a, 1b and clade 3 RBDs with nano- to picomolar affinities, and to
131 clade 2 RBDs with micro- to nanomolar affinities. The affinity of S2X259 for the Pangolin-Guanxi
132 (P-GX) RBD, however, was almost 10-fold lower compared to other clade 1b RBDs (**Extended**
133 **Data Fig. 1a**). The S2X259 Fab recognized both the SARS-CoV-2 prefusion-stabilized S
134 ectodomain trimer and the isolated SARS-CoV-2 RBD with picomolar affinity albeit with a slower
135 on-rate for binding to S presumably due to limited epitope exposure^{16,17} (**Extended Data Fig. 1a**).
136 Finally, S2X259 binding was unaffected by several point mutants or constellation of mutations
137 identified in circulating clinical isolates (K417V, N439K, Y453F, E484K) and in the B.1.1.7
138 (N501Y), B.1.351 (K417N/E484K/N501Y), B.1.427/B.1.429 (L452R), and P.1
139 (K417T/E484K/N501Y) lineage RBDs (**Fig. 1c and Extended Data Fig. 1b**).

140 We next evaluated the neutralization potency of S2X259 using authentic SARS-CoV-2-
141 Nluc as well as murine leukemia virus (MLV) and vesicular stomatitis virus (VSV) pseudotyping
142 systems. S2X259 potently neutralized authentic SARS-CoV-2, SARS-CoV-2 S MLV and SARS-
143 CoV-2 S VSV with respective half-maximal inhibitory concentrations of 144 ng/mL, 87 ng/mL
144 and 213 ng/mL (**Fig. 1d-e and Extended Data Fig. 2**). We subsequently evaluated S2X259-
145 mediated neutralization against VSV pseudotypes harboring SARS-CoV-2 S from the B.1.1.7,
146 B.1.351, P.1, and B.1.427/B.1.429 lineages of concern and the N439K or the Y453F mutation
147 identified in circulating isolates^{6,25-27}. S2X259 neutralized all of these mutants without significant
148 change in potency, in line with the identical binding affinities determined for each VOC RBD (**Fig.**
149 **1e-f and Extended Data Fig. 1b**). S2X259 further neutralized a broad panel of ACE2-utilizing
150 sarbecoviruses with comparable potencies, including SARS-CoV-2 Pangolin Guangdong (P-GD),
151 RaTG13, SARS-CoV, WIV1, WIV16 and SHC014. Finally, in line with the SPR data, S2X259
152 neutralized P-GX S VSV pseudotype but with reduced efficiency compared to SARS-CoV-2 (**Fig.**
153 **1g-h and Extended Data Fig. 1a and 2**).

154 The exceptional cross-reactivity and neutralization breadth of S2X259 against SARS-CoV-
155 2 variants and sarbecoviruses (including viruses that have not emerged in humans) indicate this
156 mAb is a promising candidate not only for COVID-19 prophylaxis or therapy but also for
157 pandemic preparedness.

158

159

160 **Structural basis for broad sarbecovirus neutralization**

161 To understand the molecular basis of S2X259-mediated broad neutralizing activity, we
162 characterized a complex between the SARS-CoV-2 S ectodomain trimer and the S2X259 Fab
163 fragment using cryo-electron microscopy (cryoEM). 3D classification of the cryoEM data showed
164 the presence of S trimers saturated with three Fabs bound to open RBDs swung out to various
165 extent for which we determined a consensus structure at 3.2 Å resolution (**Fig. 2a-b, Extended**
166 **Data Fig. 3 and Table S2**). We subsequently used local refinement to determine a 3.5 Å resolution
167 map of the region corresponding to the S2X259 variable domains and RBD, which markedly
168 improved local resolution. In parallel, we crystallized the S2X259 Fab-bound SARS-CoV-2 RBD
169 (in the presence of the S2H97 Fab²⁸) and determined a 2.65 Å resolution structure (**Fig. 2c-e and**
170 **Table S3**).

171 S2X259 recognizes a glycan-free, cryptic epitope within antigenic site IIa which was
172 previously defined based on the S2X35 mAb isolated from the same donor²¹. S2X259 binding
173 requires opening of two RBDs to grant access to the Fab in the context of the S trimer (**Fig. 2a-b**).
174 S2X259 contacts the RBD using both heavy and light chains, which contribute approximately two
175 thirds and one third of the ~950 Å² paratope surface buried upon binding, respectively.
176 Specifically, S2X259 uses complementary determining regions (CDRs) H1-H3, L1 and L3 to
177 contact RBD residues 369-386, which form two α-helices and an intervening β-strand belonging
178 to the structurally conserved RBD β-sheet, as well as the residues 404-411 and 499-508 which
179 form a continuous surface made up of an α-helix and a loop followed by an α-helix, respectively.

180 The S2X259 epitope is conserved in circulating SARS-CoV-2 isolates and does not
181 comprise prevalent RBD variants, such as S477N, N439K or L452R. S2X259 also circumvents
182 residues 417 and 484, and contacts the backbone of residue N501 but not its side chain, explaining
183 the observed high-affinity binding to the B.1.1.7, B.1.351, P.1 and B.1.429 RBDs and potent
184 neutralization of pseudotyped viruses harbouring the S glycoprotein from these VOC (**Fig. 1c, e-f**
185 **and Extended Data Fig. 1b**). S2X259-mediated broad sarbecovirus neutralization results from
186 the conservation of its epitope among sarbecovirus clades and from the angle of approach of the
187 Fab which allows it to circumvent the SARS-CoV N357 glycan present in all sarbecovirus RBDs
188 except SARS-CoV-2 (corresponding to SARS-CoV-2 residue N370) (**Extended Data Fig. 4**).
189 Neutralization of the SARS-CoV-2-related P-GX pseudotyped virus, however, is reduced ~20-fold
190 relative to SARS-CoV-2. The SARS-CoV-2 and P-GX RBDs differ at only two positions, G504N
191 and Y508F, and the structural data indicate that the former substitution would likely dampen mAb
192 binding through steric hindrance in agreement with the aforementioned binding and neutralization
193 assays (**Fig. 1h and Extended Data Fig. 1a**). The conservation of the S2X259 epitope among
194 circulating SARS-CoV-2 variants and sarbecoviruses explain the unique cross-reactivity of this
195 mAb across all sarbecovirus clades.

196 Furthermore, S2X259 binding to RBD does not affect or prevent binding by site I or site
197 IV-targeting mAbs, also defined as class 1 and 3 RBD-specific antibodies, respectively (**Extended**
198 **Data Fig. 5**), which represent the majority of antibodies currently approved or in the clinic^{21, 29-31}.
199 Therefore, S2X259 can be used in combination with these mAbs to maximize breadth against
200 currently circulating and future variants as well as to protect against potential sarbecovirus
201 introductions from animal reservoirs.

202
203

204 **S2X259 is resilient to a broad spectrum of escape mutations**

205 Motivated by the exceptional S2X259 cross-reactivity and neutralization breadth against
206 SARS-CoV-2 variants and genetically distant sarbecoviruses, we next evaluated if potential escape
207 mutations could confer resistance to this mAb. Using deep-mutational scanning (DMS) with a
208 yeast-display RBD mutant library covering all 2,034 individual amino-acid mutations that do not
209 disrupt folding or ACE2 binding^{32, 33}, we exhaustively mapped RBD mutations that escape
210 S2X259 binding. Strikingly, S2X259 binding was strongly reduced by only a restricted number of
211 amino acid substitutions, compared to previously described neutralizing mAbs³², with mutations
212 at RBD site 504 yielding the most marked reduction in binding (**Fig. 3a and Extended Data Fig.**
213 **6a-c**). Indeed, substitution of G504 with most other amino acids reduced S2X259 binding
214 compared to the wildtype (Wuhan-1) RBD, highlighting the importance of this epitope residue for
215 mAb recognition (**Fig. 3a and Extended Data Fig. 6a-c**).

216 To further explore the functional significance of the DMS data, we passaged a replication
217 competent VSV-SARS-CoV-2 chimera (in which the native S glycoprotein was replaced by the
218 SARS-CoV-2 S Wuhan-1 isolate gene^{34, 35}) in Vero cells with S2X259 mAb in the overlay. The
219 selective pressure imposed by S2X259 led to the deterministic emergence of viral mutants
220 harbouring the G504D mutation, which was the sole mutation present in each of the 18
221 neutralization-resistant plaques sampled as a result of a single nucleotide substitution from the
222 wildtype glycine codon (GGU) to an aspartate codon (GAU) (**Fig. 3b, Table S4 and Extended**
223 **Data Fig. 6d**). The selection of a single escape mutation suggests that the S2X259 epitope might
224 not tolerate amino acid changes without altering viral fitness, which could be at the basis of its
225 high conservation across the sarbecovirus subgenus.

226 The G504D substitution is very rare in circulating human SARS-CoV-2 isolates, as it has
227 been detected in only 13 out of 911,641 (0.0014%) SARS-CoV-2 genome sequences available on
228 GISAID as of April the 2nd 2021 (**Fig. 3c**). Furthermore, S2X259 efficiently neutralized VSV
229 pseudoviruses harbouring S mutations to S2X259-contact residues found with higher frequency in
230 clinical isolates (**Fig. 3c and Extended Data Fig. 6e**), in agreement with the DMS results.
231 Collectively, DMS and mAb escape selection experiments highlight the importance of position
232 G504 for S2X259-mediated neutralization. S2X259 CDRL1 and CDRL3 contact G504 or
233 surrounding residues, explaining that substituting glycine with any other (bulkier) residue prevents

234 mAb binding due to steric hindrance and the potential disruption of the interactions between the
235 Fab and residue D405, which is in close proximity to G504 (**Fig. 3d**).

236 These data also support the hypothesis proposed above for the markedly reduced affinity
237 and neutralization potency of S2X259 against the P-GX RBD and pseudotyped virus which
238 harbours the G504N mutation but maintains an aspartate at position 405 (**Fig. 1h, Extended Data**
239 **Figs. 1a, 6e and 7**). However, S2X259 binding to clade 2 S bearing G504D/E mutations (e.g.
240 Shanxi2011 or YN2013) was not abrogated (**Fig. 1c**) possibly due to substitution at the SARS-
241 CoV-2 equivalent position 405 with a serine and to substantial deletions in the RBM (**Extended**
242 **Data Fig. 7**).

243 Our results point to a high barrier for the emergence of S2X259 resistance mutants, which
244 might prove essential during the next stages of the pandemic, where increasing immune pressure
245 and continuing spread of the virus might result in the emergence of new variants.

246

247

248 **S2X259 blocks ACE2 engagement and protects Syrian hamsters from SARS-CoV-2** 249 **challenge**

250 Although S2X259 targets a conserved epitope in antigenic site II, which is distinct from
251 the RBM, some epitope residues also participate in ACE2 attachment (G502, V503 and Y505).
252 The structural data therefore indicate that S2X259 would compete with ACE2 binding to the RBD
253 (**Fig. 4a**). Accordingly, we found that S2X259 blocked binding of the SARS-CoV-2 and SARS-
254 CoV RBDs to the immobilized human recombinant ACE2 ectodomain, as measured by ELISA
255 (**Fig. 4b**).

256 Since site-II targeting mAbs conformationally select for open RBDs, we assessed if
257 S2X259 could promote shedding of the S₁ subunit from cell-surface-expressed full-length SARS-
258 CoV-2 S, as previously shown with RBD-specific mAbs isolated from SARS-CoV and SARS-
259 CoV-2-exposed individuals^{21, 36-39}. S2X259 binding efficiently promoted shedding of the S₁
260 subunit, as was the case for the RBM-targeting S2E12 mAb but not the control mAb S2M11 which
261 locks S in the prefusion closed state⁴⁰ (**Fig. 4c**). The efficient S₁ shedding induced by S2X259 is
262 responsible for the lack of FcγRIIIa and FcγRIIIa activation, which we respectively used as proxy
263 for Ab-dependent cellular phagocytosis (ADCP) and Ab-dependent cellular cytotoxicity (ADCC),
264 following incubation with target cells transiently expressing full-length SARS-CoV-2 S
265 (**Extended Data Fig. 8a-b**). Indeed, the same tests performed using target cells transfected with a
266 construct expressing an uncleavable pre-fusion stabilized SARS-CoV-2 S protein (unable to
267 release the S₁ subunit) confirmed the ability of S2X259 mAb to induce activation of FcγRIIIa and
268 FcγRIIIa in these conditions (**Extended Data Fig. 8c-d**).

269 These data show that the primary mechanism of S2X259-mediated neutralization of SARS-
270 CoV-2 and other sarbecoviruses relies on blocking viral attachment to host cell receptors through
271 competitive inhibition of ACE2 binding. Premature triggering of S₁ subunit shedding could

272 inactivate viruses before encountering target cells albeit reducing activation of S2X259 mediated
273 effector functions.

274 We next evaluated the prophylactic activity of S2X259 against challenge with the
275 prototypic (Wuhan-1 related) SARS-CoV-2 in a Syrian hamster model⁴¹. S2X259 was
276 administered via intraperitoneal injection 48h before intranasal challenge and the lungs of the
277 animals were collected 4 days later for the quantification of viral RNA and replicating virus.
278 Despite the lack of FcγRs activation *in vitro*, which has been previously ascribed with a key role
279 for protection against SARS-CoV-2^{42, 43}, S2X259 administration at 4 mg/kg reduced the amount
280 of viral RNA detected in the lungs by 1 order of magnitude compared to hamsters receiving a
281 control mAb (**Extended Data Fig 9a, c**). Furthermore, greater than 2 orders of magnitude
282 reduction in infectious virus was observed in the lungs of hamster administered with S2X259 at 4
283 mg/kg in comparison to the control group, (**Extended Data Fig. 9b, d**). We next assessed the
284 prophylactic activity of S2X259 alone and in combination with S309 against B.1.351 SARS-CoV-
285 2 challenge⁴⁴. S2X259 at 1 and 4 mg/kg or in combination with S309 (each at 1 mg/kg)
286 significantly decreased the amount of viral RNA detected in the lungs at least by 1 order of
287 magnitude in comparison to hamsters receiving a control mAb (**Fig. 4d**). Moreover, S2X259 at 4
288 mg/kg and in combination with S309 (each at 1 mg/kg) completely abrogated SARS-CoV-2
289 B.1.351 virus replication in most of the animals (**Fig. 4e**). The amounts of infectious viruses at day
290 4 detected in the group administered with only S2X259 inversely correlated with serum mAb
291 concentration measured at the time of infection (**Fig. 4f**). Animals receiving the mAb cocktail
292 appeared to benefit from the contribution of S309 or from a potential synergistic activity of the
293 two antibodies (**Fig. 4f**).

294 Overall, these results show that S2X259 protects Syrian hamsters against prototypic
295 (Wuhan-1 related) as well as B.1.351 SARS-CoV-2 replication in the lungs when prophylactically
296 administered at 4 mg/kg. Furthermore, these data demonstrate the possibility to combine S2X259
297 with S309 to maximize the beneficial activity of the two mAbs at low doses against SARS-CoV-
298 2 VOC.

299

300

301 **Discussion**

302 The uncontrolled global spread of SARS-CoV-2 has led to the detection of a large number
303 of mutations in the S glycoprotein (along with other proteins) in SARS-CoV-2 clinical isolates.
304 Some of these variants are especially concerning such as the B.1.1.7, B.1.351 and P.1 lineages
305 which originated in the UK, South Africa and Brazil, respectively^{6, 25, 27}. The independent
306 acquisition of identical or similar amino acid mutations among SARS-CoV-2 VOC has been
307 shown to abrogate or reduce the neutralization potency of a large number of mAbs and vaccine-
308 elicited sera^{7-15, 45}. Moreover, the detection of a large pool of sarbecoviruses in bats and other
309 mammals across multiple continents and the increasingly frequent interactions between humans
310 and wildlife suggests that future cross-species transmission events are likely to occur^{1, 46-49}. A

311 critical window of opportunity after a zoonotic transmission event is the prevention of viral spread
312 through deployment of effective countermeasures such as ring vaccination or administration of
313 broadly neutralizing mAbs. However, approved SARS-CoV-2 therapeutics and vaccines
314 predominantly target or elicit immunity against immunodominant but highly mutable epitopes and
315 therefore have a limited efficacy against antigenic drift and genetically distinct zoonotic strains⁴⁵.
316 ⁵⁰.

317 Strategies for eliciting broadly neutralizing and protective sarbecovirus Abs targeting the
318 RBD have recently been proposed^{22, 45} and previous work by our group and others described mAbs
319 now in the clinic with extended coverage within clade 1 sarbecoviruses^{24, 30}. Furthermore, the
320 recent results from the Phase III study demonstrating efficacy (i.e., 85%) of the cross-reactive VIR-
321 7831 mAb (a derivative of the S309 antibody) paves the way for the development of additional
322 neutralizing mAbs targeting conserved RBD epitopes that may have the dual advantage of broad
323 coverage across sarbecoviruses and of high barrier to resistance to neutralization escape.

324 Here, we identified the S2X259 mAb, that targets the RBD antigenic site II and uniquely
325 cross-reacts with all SARS-CoV-2 VOCs evaluated as well as with 30 spike trimers or RBDs from
326 all the four sarbecovirus clades. S2X259 broadly neutralizes pseudoviruses harbouring spikes from
327 the B.1.1.7, B.1.351., P.1 and B.1.427/B.1.429 lineages and from representative members of
328 SARS-CoV-2 (clade 1b) and SARS-CoV (clade 1a) strains. S2X259 neutralizes WIV1 S and
329 SHC014 S (clade 1a) pseudotyped virus that were previously suggested as potential threats to
330 human health due to their ability to replicate in human airway cell cultures and in mice^{46, 47}.
331 Moreover, S2X259 also recognizes spikes and RBDs from bat Asian (clade 2) and non-Asian
332 (clade 3) sarbecovirus clades. The coverage of clade 2 might be particularly important as Letko et
333 al.²⁰ showed that exogenous protease addition to pseudoviruses from this clade, which normally
334 do not infect human cells, could result in enhanced entry in human cells. Furthermore, although
335 clade 2 and 3 sarbecoviruses do not bind human ACE2, a recombination event following co-
336 infection by animal and human circulating strains might result in the introduction of the ACE2-
337 specific RBM within these viruses thus leading to ACE2-mediated entry^{20, 51}. The findings that
338 S2X259 not only neutralizes ACE2-using sarbecoviruses but also cross-reacts with sarbecoviruses
339 that are not known to use ACE2 indicate that this mAb is a promising candidate for clinical
340 development and could be stockpiled as part of a pandemic preparedness toolbox.

341 Based on the growing body of data demonstrating that Abs targeting the SARS-CoV-2
342 RBD account for most neutralizing activity in COVID-19 convalescent patient sera^{21, 52}, we also
343 propose that RBD-based vaccines could better promote elicitation of high titres of S2X259-like
344 neutralizing Abs due to the enhanced accessibility of its target antigenic site compared to S-based
345 vaccines^{9, 45, 53}. We anticipate these data will guide future efforts to develop SARS-CoV-2 vaccines
346 overcoming the emergence of variants as well as pan-sarbecovirus vaccines.

347

348

349

350 **ACKNOWLEDGEMENTS**

351 We thank Hideki Tani (University of Toyama) for providing the reagents necessary for preparing
352 VSV pseudotyped viruses. The authors would also like to thank also Cindy Castado and Normand
353 Blais (GSK Vaccines) for their help in the selection of the genetically divergent sarbecoviruses
354 used in this study. We thank Jay C. Nix for x-ray data collection, and Isaac Hoffman and Tristan
355 I. Croll for assistance in refinement of crystal structures. This study was supported by the National
356 Institute of General Medical Sciences (R01GM120553 to D.V.), the National Institute of Allergy
357 and Infectious Diseases (DP1AI158186 and HHSN272201700059C to D.V.; R01AI141707 to
358 J.D.B.), a Pew Biomedical Scholars Award (D.V.), Investigators in the Pathogenesis of Infectious
359 Disease Awards from the Burroughs Wellcome Fund (D.V.), Fast Grants (D.V.), the Pasteur
360 Institute (M.A.T), the Damon Runyon Cancer Research Foundation (T.N.S.) and the University of
361 Washington Arnold and Mabel Beckman cryoEM center. J.D.B. is an Investigator of the Howard
362 Hughes Medical Institute. Use of the Stanford Synchrotron Radiation Lightsource, SLAC National
363 Accelerator Laboratory, is supported by the U.S. Department of Energy, Office of Science, Office
364 of Basic Energy Sciences under Contract No. DE-AC02-76SF00515. The SSRL Structural
365 Molecular Biology Program is supported by the DOE Office of Biological and Environmental
366 Research, and by the National Institutes of Health, National Institute of General Medical Sciences
367 (P30GM133894). The contents of this publication are solely the responsibility of the authors and
368 do not necessarily represent the official views of NIGMS or NIH.

369

370

371

372 **AUTHOR CONTRIBUTIONS**

373 Experiment Design: M.A.T., N.C., T.N.S., R.M., S.P.J.W, J.D.B., D.C., D.V., and M.S.P; Donors'
374 Recruitment and Sample Collection: E.C., F.B.; PBMC Sample Processing: R.M., F.Z., A.D.M.,
375 D.P., M.B.; Protein expression and purification: M.A.T, N.C., S.J., J.E.B. K.C., N.S., C.S., I.G.,
376 and E.C.; Isolation of mAbs: R.M., F.Z., A.D.M., D.P., M.B., and C.S.F.; Binding and
377 Neutralization assays: M.A.T., A.C.W., R.M., F.Z., D.P., M.B., M.P.H., F.A.L., H.K. M.M., J.Z.,
378 and C.H.; BLI/SPR assays: A.C.W., F.Z., A.D.M, L.E.R., and E.D.; Cryo-EM Data Collection,
379 Processing, and Model Building: M.A.T, Z.W. and D.V.; ACE2 binding inhibition and S1
380 shedding: D.P. and A.D.M; Evaluation of effector functions: B.G.; Deep Mutational Scanning
381 (DMS): T.N.S., A.A., and J.D.B.; Bioinformatic analysis of virus diversity and variants: J.D.I, I.B.,
382 and A.T.; Escape mutants selection and sequencing: Z.L., and S.P.J.W.; hamster model and data
383 analysis: R.A., S.C.F., E.V., M.A.S., F.B., J.N., D.C., and M.S.P.; Data analysis: M.A.T., N.C., T.
384 N. S., A.C.W., R.M., J. D. B., D.C., D.V., and M.S.P.; Manuscript Writing: M.A.T., N.C., T.N.S.,
385 R.M., J.N., A.T., G.S., H.W.V, S.P.J.W, J.D.B., D.C., D.V., and M.S.P.; Supervision: F.A.L.,
386 L.E.R., C. H., M.A.S., F.B., E.C., J.N., A.T., G.S., H.W.V, S.P.J.W, J.D.B., D.C., D.V., and
387 M.S.P.; Funding Acquisition: J. D. B., D.V.

388

389

390

391 **DECLARATION OF INTERESTS**

392 N.C., R.M., F.Z., S.J., J.D.I., A.D.M., D.P., M.B., I.B., M.H., F.A.L., L.E.R., E.D., H. K., M.M,
393 J.Z., K.C., N.S., C.S., E.V., I.G., C.S.F., C.H., M.A.S., F.B., E.C., A.T., G.S., H.W.V., D.C., and
394 M.S.P. are employees of Vir Biotechnology Inc. and may hold shares in Vir Biotechnology Inc.
395 D.C. is currently listed as an inventor on multiple patent applications, which disclose the subject
396 matter described in this manuscript. The Neyts laboratories have received sponsored research
397 agreements from Vir Biotechnology Inc. H.W.V. is a founder of PierianDx and Casma
398 Therapeutics. Neither company provided funding for this work or is performing related work. D.V.
399 is a consultant for Vir Biotechnology Inc. The Veessler laboratory has received a sponsored
400 research agreement from Vir Biotechnology Inc. The remaining authors declare that the research
401 was conducted in the absence of any commercial or financial relationships that could be construed
402 as a potential conflict of interest.

403

404

405

406 **MATERIALS AND METHODS**

407

408 **Cell lines**

409 Cell lines used in this study were obtained from ATCC (HEK293T, Vero and Vero-E6),
410 ThermoFisher Scientific (Expi CHO cells, FreeStyle™ 293-F cells and Expi293F™ cells) or were
411 generated via lentiviral transduction (Expi CHO-S, HEK293T-ACE2).

412

413 **Sample donors**

414 Samples from a SARS-CoV-2 recovered individual, designated as donor X (male, 52 years-
415 old), was obtained 75 days after symptoms onset under study protocols approved by the local
416 Institutional Review Boards (Canton Ticino Ethics Committee, Switzerland, the Ethical committee
417 of Luigi Sacco Hospital, Milan, Italy). The donor provided written informed consent for the use
418 of blood and blood components (e.g. PBMCs, sera or plasma).

419

420 **Isolation of peripheral blood mononuclear cells (PBMCs), plasma and sera**

421 PBMCs were isolated from blood draw performed using tubes pre-filled with heparin, followed by
422 Ficoll density gradient centrifugation. PBMCs were either used freshly along SARS-CoV2 Spike
423 protein specific memory B cells sorting or stored in liquid nitrogen for later use. Sera were obtained
424 from blood collected using tubes containing clot activator, followed by centrifugation and stored
425 at -80 °C.

426

427 **B-cell isolation and recombinant S2X259 mAb production**

428 Starting from freshly isolated PBMCs or upon cells thawing, B cells were enriched by staining
429 with CD19 PE-Cy7 and incubation with anti-PE beads, followed by positive selection using LS
430 columns. Enriched B cells were stained with anti-IgM, anti-IgD, anti-CD14 and anti-IgA, all PE

431 labelled, and prefusion SARS-CoV-2 S with a biotinylated avi tag conjugated to Streptavidin
432 Alexa-Fluor 647 (Life Technologies). SARSCoV-2 S-specific IgG⁺ memory B cells were sorted
433 by flow cytometry via gating for PE negative and Alexa-Fluor 647 positive cells. Cells were
434 cultured for the screening of positive supernatants. Antibody VH and VL sequences were obtained
435 by RT-PCR and mAbs were expressed as recombinant human Fab fragment or as IgG1 (G1m3
436 allotype). ExpiCHO cells were transiently transfected with heavy and light chain expression
437 vectors as previously described³⁰.

438 Affinity purification was performed on ÄKTA Xpress FPLC (Cytiva) operated by UNICORN
439 software version 5.11 (Build 407) using HiTrap Protein A columns (Cytiva) for full length human
440 and hamster mAbs and CaptureSelect CH1-XL MiniChrom columns (ThermoFisher Scientific)
441 for Fab fragments, using PBS as mobile phase. Buffer exchange to the appropriate formulation
442 buffer was performed with a HiTrap Fast desalting column (Cytiva). The final products were
443 sterilized by filtration through 0.22 µm filters and stored at 4 °C.

444

445 **Sarbecovirus sequence analysis and SARS-CoV-2 mutant counts**

446 Alignment and phylogenetic tree of the strains within the sarbecovirus subgenus was generated
447 using MEGA 7.0.26 and CLC Main workbench 21.0.3 (Qiagen). The following sequences were
448 retrieved from GISAID and NCBI: A021 (AAV97986.1); HKU3 (QND76020.1); WIV1
449 (AGZ48831.1); Rs3367 (AGZ48818.1); Anlong-112 (ARI44804.1); RsSHC014 (AGZ48806.1);
450 Rs4081 (AGZ48798.1); YN2013 (AIA62330.1); Rs4874 (ATO98205.1); Rs4255 (ATO98193.1);
451 Rs4231 (ATO98157.1); Rs4084 (ATO98132.1); ZXC21 (AVP78042.1); SC2018 (QDF43815.1);
452 ZC45 (AVP78031.1); Rp/Shaanxi2011 (AGC74165.1); Rm1/2004 (ABD75332.1); Rf1-2004
453 (ABD75323.1); Rf4092 (ATO98145.1); BM48-31/BGR/2008 (YP_003858584.1); LYRa11
454 (AHX37558.1); RaTG13 (QHR63300.2); PC4-127 (AAU93318.1); CS24 (ABF68959.1); SARS-
455 CoV2 (YP_009724390.1); LYRa3 (AHX37569.1); Cp/Yunnan2011 (AGC74176.1); SARS
456 coronavirus Urbani (AAP13441.1); As6526 (ATO98108.1); BtkY72 (APO40579.1); RmYN02
457 (EPI_ISL_412977); Pangolin_Guangdong-2019 (EPI_ISL_410721); Pangolin-Guanxi-2017
458 (EPI_ISL_410539).

459 The viral sequences were obtained from GISAID EpiCoV project (<https://www.gisaid.org/>).
460 Analysis was performed on sequences submitted to GISAID up to April 2nd, 2021. The spike
461 protein sequences were either obtained directly from the protein dump provided by GISAID or,
462 for the latest submitted sequences that were not incorporated yet in the protein dump at the day of
463 data retrieval, from the genomic sequences with *exonerate*⁵⁴ 2.2.4.0--haf93ef1_3
464 (<https://quay.io/repository/biocontainers/exonerate?tab=tags>) using protein to DNA alignment
465 with parameters *-m protein2dna --refine full --minintron 999999 --percent 20* and using
466 accession [YP_009724390.1](https://www.ncbi.nlm.nih.gov/nuccore/YP_009724390.1) as a reference. Multiple sequence alignment of all human spike
467 proteins was performed with *mafft*⁵⁵ 7.475--h516909a_0
468 (<https://quay.io/repository/biocontainers/mafft?tab=tags>) with parameters *--auto --reorder --*
469 *keeplength --addfragments* using the same reference as above. Spike sequences that contained
470 >10% ambiguous amino acid or that were < than 80% of the canonical protein length were

471 discarded. A total of 923,686 sequences were used for analysis. Variants were then extracted as
472 compared to the reference with R 4.0.2 (<https://www.r-project.org/>) using Biostrings 2.56.0.

473

474 **Binding to cell surface expressed Sarbecovirus S proteins by Flow Cytometry**

475 ExpiCHO-S cells were seeded at 6×10^6 cells/mL in a volume of 5 mL in a 50 mL bioreactor.
476 Spike encoding plasmids HKU3 (QND76020.1), Rs3367 (AGZ48818.1), YN2013 (AIA62330.1),
477 Rs4874 (ATO98205.1), Rs4255 (ATO98193.1), Rs4231 (ATO98157.1), Rs4084 (ATO98132.1),
478 ZXC21 (AVP78042.1), ZC45 (AVP78031.1), Rp/Shaanxi2011 (AGC74165.1), Rm1/2004
479 (ABD75332.1), Rf1-2004 (ABD75323.1), BM48-31/BGR/2008 (YP_003858584.1), RaTG13
480 (QHR63300.2), PC4-127 (AAU93318.1), SARS-CoV2 (YP_009724390.1), LYRa3
481 (AHX37569.1), Cp/Yunnan2011 (AGC74176.1), SARS-CoV Urbani (AAP13441.1), As6526
482 (ATO98108.1), BtKY72 (APO40579.1), RmYN02 (EPI_ISL_412977), Pangolin_Guangdong-
483 2019 (EPI_ISL_410721), Pangolin-Guanxi-2017 (EPI_ISL_410539), HKU3-12 (ADE34812.1)
484 were diluted in cold OptiPRO SFM (Life Technologies, 12309-050), mixed with ExpiFectamine
485 CHO Reagent (Life Technologies, A29130) and added to the cells. Transfected cells were then
486 incubated at 37°C with 8% CO₂ with an orbital shaking speed of 250 RPM (orbital diameter of 25
487 mm) for 42 hours. Transiently transfected ExpiCHO cells were harvested and washed two times
488 in wash buffer (PBS 2% FBS, 2 mM EDTA). Cells were counted and distributed into round bottom
489 96-well plates (Corning, 3799) and incubated with 10 µg/ml of S2X259 mAb. Alexa Fluor647-
490 labelled Goat Anti-Human IgG secondary Ab (Jackson ImmunoResearch, 109-606-098) was
491 prepared at 2 µg/ml and added onto cells after two washing steps. Cells were then washed twice
492 and resuspended in wash buffer for data acquisition at ZE5 cytometer (Biorad).

493

494 **Recombinant protein production**

495 Wild-type SARS-CoV-2 RBD (with N-terminal signal peptide and 'ETGT', and C-terminal 8xHis-
496 tag) was expressed in Expi293F cells at 37°C and 8% CO₂ in the presence of 10 µM kifunensine.
497 Transfection was performed using the ExpiFectamine 293 Transfection Kit (Thermo Fisher
498 Scientific). Cell culture supernatant was collected four days after transfection and supplemented
499 with 10x PBS to a final concentration of 2.5x PBS (342.5 mM NaCl, 6.75 mM KCl and 29.75 mM
500 phosphates). For crystallization, wild-type SARS-CoV-2 RBD was purified using a 5 mL
501 HisTALON superflow cartridge (Takara Bio) followed by size exclusion chromatography using a
502 Superdex 200 10/300 GL column pre-equilibrated in 20 mM Tris-HCl pH 7.5, 150 mM NaCl.
503 RBD was deglycosylated with EndoH and mixed with a 1.3-fold molar excess of S2X259 Fab and
504 S309 Fab. The complex was purified on a Superdex 200 10/300 GL column pre-equilibrated with
505 20 mM Tris-HCl pH 7.5, 150 mM NaCl. SARS-CoV-2 S hexaprotein, used for cryo-EM single
506 particle studies, was expressed and purified as described before⁴⁰.

507

508 **Enzyme-linked immunosorbent assay (ELISA)**

509 96 half area well-plates (Corning, 3690) were coated over-night at 4°C with 25 µl of
510 sarbecoviruses RBD proteins WIV1 (AGZ48831.1), Anlong-112 (ARI44804.1), YN2013

511 (AIA62330.1), SC2018 (QDF43815.1), ZC45 (AVP78031.1), Rp/Shaanxi2011 (AGC74165.1),
512 BM48-31/BGR/2008 (YP_003858584.1), RaTG13 (QHR63300.2), SARS-CoV2
513 (YP_009724390.1), SARS-CoV Urbani (AAP13441.1), BtKY72 (APO40579.1),
514 Pangolin_Guangdong-2019 (EPI_ISL_410721) and SARS-CoV-2 RBD mutants, prepared at 5
515 $\mu\text{g/ml}$ in PBS pH 7.2. Plates were then blocked with PBS 1% BSA (Sigma-Aldrich, A3059) and
516 subsequently incubated with mAb serial dilutions for 1 h at room temperature. After 4 washing
517 steps with PBS 0.05% Tween 20 (PBS-T) (Sigma-Aldrich, 93773), goat anti-human IgG secondary
518 antibody (Southern Biotech, 2040-04) was added and incubated for 1 h at room temperature. Plates
519 were then washed 4 times with PBS-T and 4-NitroPhenyl phosphate (pNPP, Sigma-Aldrich,
520 71768) substrate was added. After 30 min incubation, absorbance at 405 nm was measured by a
521 plate reader (Biotek) and data plotted using Prism GraphPad.

522

523 **MLV-based pseudotyped virus production and neutralization**

524 To generate SARS-CoV-2 S murine leukemia virus pseudotyped virus, HEK293T cells were
525 seeded in 10-cm dishes in DMEM supplemented with 10% FBS. The next day cells were
526 transfected with a SARS-CoV-2 S glycoprotein-encoding plasmid harbouring the D19 C-terminal
527 truncation⁵⁶, an MLV Gag-Pol packaging construct and the reporter vector pTG-Luc, using the
528 X-tremeGENE HP DNA transfection reagent (Roche) according to the manufacturer's
529 instructions. Cells were then incubated at 37°C with 5% CO₂ for 72 h. Supernatant was harvested
530 and cleared from cellular debris by centrifugation at 400 x g, and stored at -80 °C.

531 For neutralization assays, Vero E6 cells were seeded into white 96-well plates (PerkinElmer) at
532 20,000 cells/well and cultured overnight at 37 °C with 5 % CO₂ in 100 μl DMEM supplemented
533 with 10% FBS and 1% penicillin/streptomycin. The next day, MLV-SARS-CoV-2 pseudovirus
534 was activated with 10 $\mu\text{g/ml}$ TPCK treated-Trypsin (Worthington Biochem) for 1 h at 37 °C.
535 Recombinant antibodies at various concentrations were incubated with activated pseudovirus for
536 1 h at 37 °C. The Vero E6 cells were then washed with DMEM, and 50 μl of pseudovirus/mAbs
537 mixes were added and incubated for 2 h at 37 °C with 5 % CO₂. After incubation, 50 μl of DMEM
538 containing 20% FBS and 2 % penicillin/streptomycin were added and the cells were incubated 48
539 h at 37 °C with 5 % CO₂. Following these 48 h of infection, culture medium was removed from
540 the cells and 50 $\mu\text{l/well}$ of Bio-Glo (Promega) diluted 1:2 with PBS with Ca²⁺Mg²⁺ (Thermo
541 Fisher) was added to the cells and incubated in the dark for 15 min before reading on a Synergy
542 H1 Hybrid Multi-Mode plate reader (Biotek). Measurements were done in duplicate, RLU values
543 were converted to percentage of neutralization and plotted with a nonlinear regression curve fit in
544 Graph Prism.

545 **VSV-based pseudotype virus production and neutralization assay**

546 SARS-CoV-2 S (CAD0240757.1), RaTG13 S (QHR63300.2), Pangolin-Guangdong
547 S(QLR06867.1), Pangolin-Guanxi S (QIA48623.1), SARS-CoV S (YP 009825051.1), WIV1 S
548 (AGZ48831.1), WIV16 S (ALK02457.1), RsSHCO14 S (AGZ48806.1), the VOC B.1.429 S
549 (QTC60823) and the VOCs, N437K, Y453F, B.1.1.7 S, B.1.351 S and P.1 S with their
550 corresponding mutations inserted in the SARS-CoV-2 S (CAD0240757.1) backbone were used to

551 pseudotype VSV. Pseudotyped viruses were prepared using 293T cells seeded in 10-cm dishes.
552 Briefly, cells in DMEM supplemented with 10% FBS, 1% PenStrep were transfected with the
553 plasmid encoding for the corresponding S glycoprotein using lipofectamine 2000 (Life
554 Technologies) following manufacturer's indications. One day post-transfection, cells were
555 infected with VSV (G*ΔG-luciferase) and after 2 h, infected cells were washed four times with
556 DMEM before adding medium supplemented with anti-VSV-G antibody (I1- mouse hybridoma
557 supernatant diluted 1 to 50, from CRL- 2700, ATCC). Particles were harvested 18 h post-
558 inoculation, clarified from cellular debris by centrifugation at 2,000 x g for 5 min and concentrated
559 10 times using a 30 kDa cut off membrane and used for neutralization experiments, aliquoted and
560 frozen at -80°C until use in neutralization experiments.
561 For neutralization, stable 293T cells expressing ACE2⁵⁷ in DMEM supplemented with 10% FBS,
562 1% PenStrep were seeded at 40,000 cells/well into clear bottom white walled 96-well plates and
563 cultured overnight at 37°C. Twelve-point 3-fold serial dilutions of the corresponding mAb were
564 prepared in DMEM and pseudotyped VSV viruses were added 1:1 to each mAb dilution in the
565 presence of anti-VSV-G antibody from I1- mouse hybridoma supernatant diluted 50 times. After
566 45 min incubation at 37°C, 40 μl of the mixture was added to the cells and 2 h post-infection, 40
567 μL DMEM was added to the cells. After 17-20 h 50 μL/well of One-Glo-EX substrate (Promega)
568 was added to the cells and incubated in the dark for 5-10 min prior reading on a Varioskan LUX
569 plate reader (ThermoFisher). Measurements were done in duplicate with two independent
570 productions of pseudotyped viruses and RLU values were converted to percentage of
571 neutralization and plotted with a nonlinear regression curve fit in Graph Prism.

572 **Neutralization of authentic SARS-CoV-2-Nluc virus**

573 Neutralization of authentic SARS-CoV-2 by entry-inhibition assay was determined using SARS-
574 CoV-2-Nluc, an infectious clone of SARSCoV-2 (based on strain 2019-nCoV/USA_WA1/2020)
575 which encodes nanoluciferase in place of the viral ORF7 and demonstrated comparable growth
576 kinetics to wildtype virus⁵⁸. Vero E6 cells were seeded into black-walled, clear-bottom 96-well
577 plates at 2 x 10⁴ cells/well and cultured overnight at 37 °C. The next day, 9-point 4-fold serial
578 dilutions of mAbs were prepared in infection media (DMEM + 10% FBS). SARS-CoV-2-Nluc
579 was diluted in infection media at a final MOI of 0.01 PFU/cell, added to the mAb dilutions and
580 incubated for 30 minutes at 37 °C. Media was removed from the Vero E6 cells, mAb-virus
581 complexes were added and incubated at 37 °C for 24 hours. Media was removed from the cells,
582 Nano-Glo luciferase substrate (Promega) was added according to the manufacturer's
583 recommendations, incubated for 10 minutes at room temperature and the luciferase signal was
584 quantified on a VICTOR Nivo plate reader (Perkin Elmer).

585

586 **Affinity determination by Surface Plasmon Resonance (SPR)**

587 SPR binding measurements were performed using a Biacore T200 instrument using either anti-
588 AviTag pAb (for capturing S proteins) or StrepTactin XT (for capturing RBDs) covalently
589 immobilized on CM5 chips. Running buffer was Cytiva HBS-EP+ (pH 7.4). All measurements
590 were performed at 25 °C. S2X259 Fab concentrations were 11, 33, 100, and 300 nM run as single-

591 cycle kinetics. Double reference-subtracted data were fit to a 1:1 binding model using Biacore
592 Evaluation software, which yields an “apparent K_D ” for the S-binding data because the kinetics
593 also reflect S conformational dynamics. For SARS-CoV-2 S the dissociation rate was too slow to
594 fit, so the $K_{D,app}$ is reported as an upper limit. The K_D above 1 μM is approximate and was
595 determined from a fit where R_{max} was set to a constant based on theoretical R_{max} .

596

597 **Affinity determination using bio-layer interferometry**

598 Biotinylated RBD (WT, N501Y, K417N-E484K-N501Y, or K417T-E484K-N501Y) were
599 immobilized at 5 ng/ μL in undiluted 10X Kinetics Buffer (Pall) to SA sensors until a load level of
600 1.1nm. A 1:3 dilution series of Fab in undiluted kinetics buffer starting at 10nM was used for 600
601 seconds association prior to 600 second dissociation to determine protein-protein affinity. The data
602 were baseline subtracted and the plots fitted using the Pall FortéBio/Sartorius analysis software
603 (version 12.0). Data were plotted in Prism.

604

605 **Competition assay by Biolayer Interferometry (BLI)**

606 BLI was used to assess S2X259 competition with S309 and S2E12 using an Octet Red96
607 (ForteBio). All reagents were prepared in kinetics buffer (PBS 0.01% BSA) at the indicated
608 concentrations. His-tagged SARS-CoV-2 RBD was prepared at 8 $\mu\text{g}/\text{ml}$ and loaded on pre-
609 hydrated anti-penta-HIS biosensors (Sartorius) for 2.5 min. Biosensors were then moved into a
610 solution containing S2X259 mAb and association recorded for 7 min. A second association step
611 was subsequently performed into S2X259 (as control), S309 and S2E12 mAbs solutions at 20
612 $\mu\text{g}/\text{ml}$ and recorded for 7 min. Response values were exported and plotted using GraphPad Prism.

613

614 **Cell-surface mAb-mediated S_1 shedding**

615 CHO cells stably expressing wild-type SARS-CoV-2 S were resuspended in wash buffer (PBS 1
616 % BSA, 2 mM EDTA) and treated with 10 $\mu\text{g}/\text{mL}$ TPCK-trypsin (Worthington Biochem) for 30
617 min at 37°C. Cells were then washed and distributed into round bottom 96-well plates (90,000
618 cells/well). S2X259 was added to cells at 15 $\mu\text{g}/\text{mL}$ final concentration for 180 min at 37 °C. Cells
619 were collected at different time points (5, 30, 60, 120 and 180), washed with wash buffer at 4 °C,
620 and incubated with 1.5 $\mu\text{g}/\text{mL}$ secondary goat anti-human IgG, Fc fragment specific (Jackson
621 ImmunoResearch) on ice for 20 min. Cells were washed and resuspended in wash buffer and
622 analyzed with ZE5 FACS (Bio-rad).

623

624 **Measurement of Fc-effector functions**

625 S2X259-dependent activation of human Fc γ RIIIa was performed with a bioluminescent reporter
626 assay. ExpiCHO cells transiently expressing full-length wild-type SARS-CoV-2 S (target cells) or
627 full-length prefusion stabilized SARS-CoV-2 S, which harbours the 2P mutation and S1/S2 furin
628 cleavage site mutation (RRARS to SGAG) as previously described¹⁶, were incubated with different
629 amounts of mAbs. After a 15-minute incubation, Jurkat cells stably expressing Fc γ RIIIa receptor
630 (V158 variant) or Fc γ RIIIa receptor (H131 variant) and NFAT-driven luciferase gene (effector

631 cells) were added at an effector to target ratio of 6:1 for FcγRIIIa and 5:1 for FcγRIIa. Signaling
632 was quantified by the luciferase signal produced as a result of NFAT pathway activation.
633 Luminescence was measured after 20 hours of incubation at 37°C with 5% CO₂ with a
634 luminometer using the Bio-Glo-TM Luciferase Assay Reagent according to the manufacturer's
635 instructions (Promega).

636

637 **In vivo mAb testing using a Syrian hamster model**

638 KU LEUVEN R&D has developed and validated a SARS-CoV-2 Syrian Golden hamster infection
639 model ^{41, 44}. The SARS-CoV-2 Wuhan (BetaCov/Belgium/GHB-03021/2020-EPI_ISL_109
640 407976|2020-02-03) and B.1.351 (hCoV105_19/Belgium/regal-1920/2021; EPI_ISL_896474,
641 2021-01-11) isolates used in this study, were recovered from nasopharyngeal swabs taken from a
642 RT-qPCR confirmed asymptomatic patient who returned from Wuhan, China in February 2020
643 and from a patient with respiratory symptoms returned to Belgium in January 2021, respectively.
644 A close relatedness with the prototypic Wuhan-Hu-1 2019 SARS-CoV-2 and with B.1.351 lineage
645 was confirmed by sequencing and phylogenetic analysis. Infectious viruses were isolated by serial
646 passaging on Vero E6 cells and passage 6 for SARS-CoV-2 Wuhan and passage 2 for B.1.351
647 viruses were used for the study. The titre of the virus stock was determined by end-point dilution
648 on Vero E6 cells by the Reed and Muench method ⁵⁹. This work was conducted in the high-
649 containment A3 and BSL3+ facilities of the KU Leuven Rega Institute (3CAPS) under licenses
650 AMV 30112018 SBB 219 2018 0892 and AMV 23102017 SBB 219 20170589 according to
651 institutional guidelines.

652 Syrian hamsters (*Mesocricetus auratus*) were purchased from Janvier Laboratories and were
653 housed per two in ventilated isolator cages (IsoCage N Biocontainment System, Tecniplast) with
654 ad libitum access to food and water and cage enrichment (wood block). Housing conditions and
655 experimental procedures were approved by the ethical committee of animal experimentation of
656 KU Leuven (license P065-2020). 6-10 week-old female hamsters were administered by
657 intraperitoneal injection with S2X259 mAb at 1 mg/kg and 4 mg/kg 48 hours before intranasal
658 infection with 1.89×10⁶ TCID₅₀ in 50 µl inoculum. Hamsters were monitored for appearance,
659 behavior and weight. At day 4 post infection hamsters were euthanized by intraperitoneal injection
660 of 500 µL Dolethal (200 mg/mL sodium pentobarbital, Vétoquinol SA). Lungs were collected,
661 homogenized using bead disruption (Precellys) in 350 µL RLT buffer (RNeasy Mini kit, Qiagen)
662 and centrifuged (10,000 rpm, 5 minutes, 4°C) to pellet the cell debris. RNA was extracted using a
663 NucleoSpin kit (Macherey-Nagel) according to the manufacturer's instructions. RT-qPCR was
664 performed on a LightCycler96 platform (Roche) using the iTaq Universal Probes One-Step
665 RTqPCR kit (BioRad) with N2 primers and probes targeting the nucleocapsid ⁴¹. Standards of
666 SARS-CoV-2 cDNA (IDT) were used to express viral genome copies per mg tissue or per mL
667 serum. To quantify infectious SARS-CoV-2 particles, endpoint titrations were performed on
668 confluent Vero E6 cells in 96-well plates. Viral titres were calculated by the Reed and Muench
669 method ⁵⁹ and were expressed as 50% tissue culture infectious dose (TCID₅₀) per mg tissue.

670

671 **Evaluation of escape mutants via deep mutational scanning (DMS)**

672 A previously described deep mutational scanning approach³² was used to identify RBD mutations
673 that escape S2X259 binding. Briefly, duplicate libraries containing virtually all possible amino
674 acid changes compatible with ACE2 binding and RBD folding within the Wuhan-Hu-1 SARS-
675 CoV-2 RBD sequence were expressed on the surface of yeast^{32, 33}. Libraries were labelled at 59
676 ng/mL S2X259 antibody (the EC90 for binding to yeast-displayed SARS-CoV-2 RBD determined
677 in isogenic pilot binding experiments), and fluorescence-activated cell sorting (FACS) was used
678 to select RBD⁺ cells that exhibit reduced antibody binding as previously described^{32, 60}. See FACS
679 plots in Extended Data Fig. 6a. Libraries were sequenced before and after selection to determine
680 per-mutation escape fractions as previously described⁶⁰. Experiments were performed in duplicate
681 with independently generated mutant libraries (correlations shown in Extended Data Fig. 6b), and
682 we report the average mutant escape fraction across the duplicates. Raw escape fractions are
683 available on GitHub: [https://github.com/jbloomlab/SARS-CoV-2-](https://github.com/jbloomlab/SARS-CoV-2-RBD_MAP_Vir_mAbs/blob/main/results/supp_data/s2X259_raw_data.csv)
684 [RBD_MAP_Vir_mAbs/blob/main/results/supp_data/s2X259_raw_data.csv](https://github.com/jbloomlab/SARS-CoV-2-RBD_MAP_Vir_mAbs/blob/main/results/supp_data/s2X259_raw_data.csv). Detailed steps of
685 analysis and code for the deep mutational scanning selections are available on GitHub:
686 https://github.com/jbloomlab/SARS-CoV-2-RBD_MAP_Vir_mAbs.

687

688 **Selection of SARS-CoV-2 monoclonal antibody escape mutants (MARMS)**

689 VSV-SARS-CoV-2 chimera was used to select for SARS-CoV-2 S monoclonal antibody resistant
690 mutants (MARMS) previously described (^{34, 35}). Briefly, MARMS were recovered by plaque
691 isolation on Vero cells with the indicated mAb in the overlay. The concentration of mAb in the
692 overlay was determined by neutralization assays at a multiplicity of infection (MOI) of 100. Escape
693 clones were plaque-purified on Vero cells in the presence of mAb, and plaques in agarose plugs
694 were amplified on MA104 cells with the mAb present in the medium. Viral stocks were amplified
695 on MA104 cells at an MOI of 0.01 in Medium 199 containing 2% FBS and 20 mM HEPES pH
696 7.7 (Millipore Sigma) at 34°C. Viral supernatants were harvested upon extensive cytopathic effect
697 and clarified of cell debris by centrifugation at 1,000 x g for 5 min. Aliquots were maintained at -
698 80°C. Viral RNA was extracted from VSV-SARS-CoV-2 mutant viruses using RNeasy Mini kit
699 (Qiagen), and S was amplified using OneStep RT-PCR Kit (Qiagen). The mutations were
700 identified by Sanger sequencing (GENEWIZ). Their resistance was verified by subsequent virus
701 infection in the presence or absence of antibody. Briefly, Vero cells were seeded into 12 well plates
702 for overnight. The virus was serially diluted using DMEM and cells were infected at 37°C for 1 h.
703 Cells were cultured with an agarose overlay in the presence or absence of mAb at 34°C for 2 days.
704 Plates were scanned on a biomolecular imager and expression of eGFP is show at 48 hours post-
705 infection.

706

707 **Crystallization, data collection, structure determination and analysis**

708 Crystals of the SARS-CoV-2-RBD-S2X259-S2H97 Fab complex were obtained at 20°C by sitting
709 drop vapor diffusion. A total of 200 nL complex at 5.7 mg/ml were mixed with 200 nL mother
710 liquor solution containing 0.12 M Monosaccharides mix, 20% (v/v) Ethylene glycol, 10% (w/v)

711 PEG 8000, 0.1 M Tris (base)/bicine pH 8.5, 0.02 M Sodium chloride, 0.01 M MES pH 6 and 3%
712 (v/v) Jeffamine ED-2003. Crystals were flash frozen in liquid nitrogen. Data were collected at
713 Beamline 9-2 of the Stanford Synchrotron Radiation Lightsource facility in Stanford, CA. Data
714 were processed with the XDS software package⁶¹ for a final dataset of 2.65 Å in space group P21.
715 The RBD-S2X259-S2H97 Fab complex structure was solved by molecular replacement using
716 phaser⁶² from a starting model consisting of SARS-CoV-2 RBD (PDB ID: 7JX3) and homology
717 models of the S2X259 and S2H97 Fabs built using the Molecular Operating Environment (MOE)
718 software package from the Chemical Computing Group (<https://www.chemcomp.com>). Several
719 subsequent rounds of model building and refinement were performed using Coot⁶³, ISOLDE⁶⁴,
720 Refmac⁶⁵, and MOE (<https://www.chemcomp.com>), to arrive at a final model for the ternary
721 complex.

722

723 **CryoEM sample preparation, data collection and data processing**

724 Recombinantly expressed and purified fab S2X259 and SARS-CoV-2 S hexaprotein were incubated
725 at 1 mg/ml with a 1.2 molar excess of fab at 4°C during 1 hr. Three microliters of the complex
726 mixture were loaded onto freshly glow discharged R 2/2 UltrAuFoil grids (200 mesh) or lacey
727 grids covered with a thin layer of manually added carbon, prior to plunge freezing using a vitrobot
728 MarkIV (ThermoFisher Scientific) with a blot force of 0 and 7-7.5 sec blot time (for the UltrAuFoil
729 grids) or with a blot force of -1 and 2.5 sec blot time (for the lacey thin carbon grids) at 100 %
730 humidity and 21°C.

731 Data were acquired on a FEI Titan Krios transmission electron microscope operated at 300 kV and
732 equipped with a Gatan K2 Summit direct detector and Gatan Quantum GIF energy filter, operated
733 in zero-loss mode with a slit width of 20 eV. Automated data collection was carried out using
734 Legion⁶⁶ at a nominal magnification of 130,000x with a super-resolution pixel size of 0.525 Å.
735 The dose rate was adjusted to 8 counts/pixel/s, and each movie was fractionated in 50 frames of
736 200 msec. Two datasets were collected from UltrAuFoil grids with the stage tilted 30° and 55° to
737 circumvent particle preferential orientation. The third dataset was collected on lacey grids covered
738 with a thin layer of carbon. The three datasets, with a total of 6786 micrographs, were collected
739 with a defocus range comprised between -0.8 and -2 µm. For each dataset, movie frame alignment,
740 estimation of the microscope contrast-transfer function parameters, particle picking and extraction
741 were carried out using Warp⁶⁷. Particle images were extracted with a box size of 800 pixels² and
742 binned to 400 yielding a pixel size of 1.05 Å. The three datasets were merged and two rounds of
743 reference-free 2D classification were performed using cryoSPARC⁶⁸. Subsequently, one round of
744 3D classification with 50 iterations, using PDB 6VXX as initial model, was carried out using
745 Relion^{69, 70} without imposing symmetry. 3D refinements were carried out using non-uniform
746 refinement⁷¹. Particle images from each dataset were subjected to Bayesian polishing⁷² using
747 Relion before merging them to perform another round of non-uniform refinement in cryoSPARC
748 followed by per-particle defocus refinement and again non-uniform refinement. To improve the
749 density of the S/S2X259 interface, the particles were symmetry-expanded and subjected to a
750 Relion focus 3D classification without refining angles and shifts using a soft mask encompassing

751 the RBD and S2X259 variable domains. Particles belonging to classes with the best resolved local
752 density were selected and subjected to local refinement using cryoSPARC. Local resolution
753 estimation, filtering, and sharpening were carried out using CryoSPARC. Reported resolutions are
754 based on the gold-standard Fourier shell correlation (FSC) of 0.143 criterion and Fourier shell
755 correlation curves were corrected for the effects of soft masking by high-resolution noise
756 substitution⁷³.

757

758 **CryoEM model building and analysis.**

759 UCSF Chimera⁷⁴ and Coot⁶³ were used to fit atomic models (PDB 6VXX or PDB 6VYB) into the
760 cryoEM maps and the Fab variable domains were manually built. S2E12 was built in the locally
761 refined map and subsequently validated using the Fab crystal structure. Models were refined and
762 relaxed using Rosetta using both sharpened and unsharpened maps^{75,76}. Validation used Phenix⁷⁷,
763 Molprobit⁷⁸ and Privateer⁷⁹. Figures were generated using UCSF ChimeraX⁸⁰.

764

765

766

767

768

769

770

771

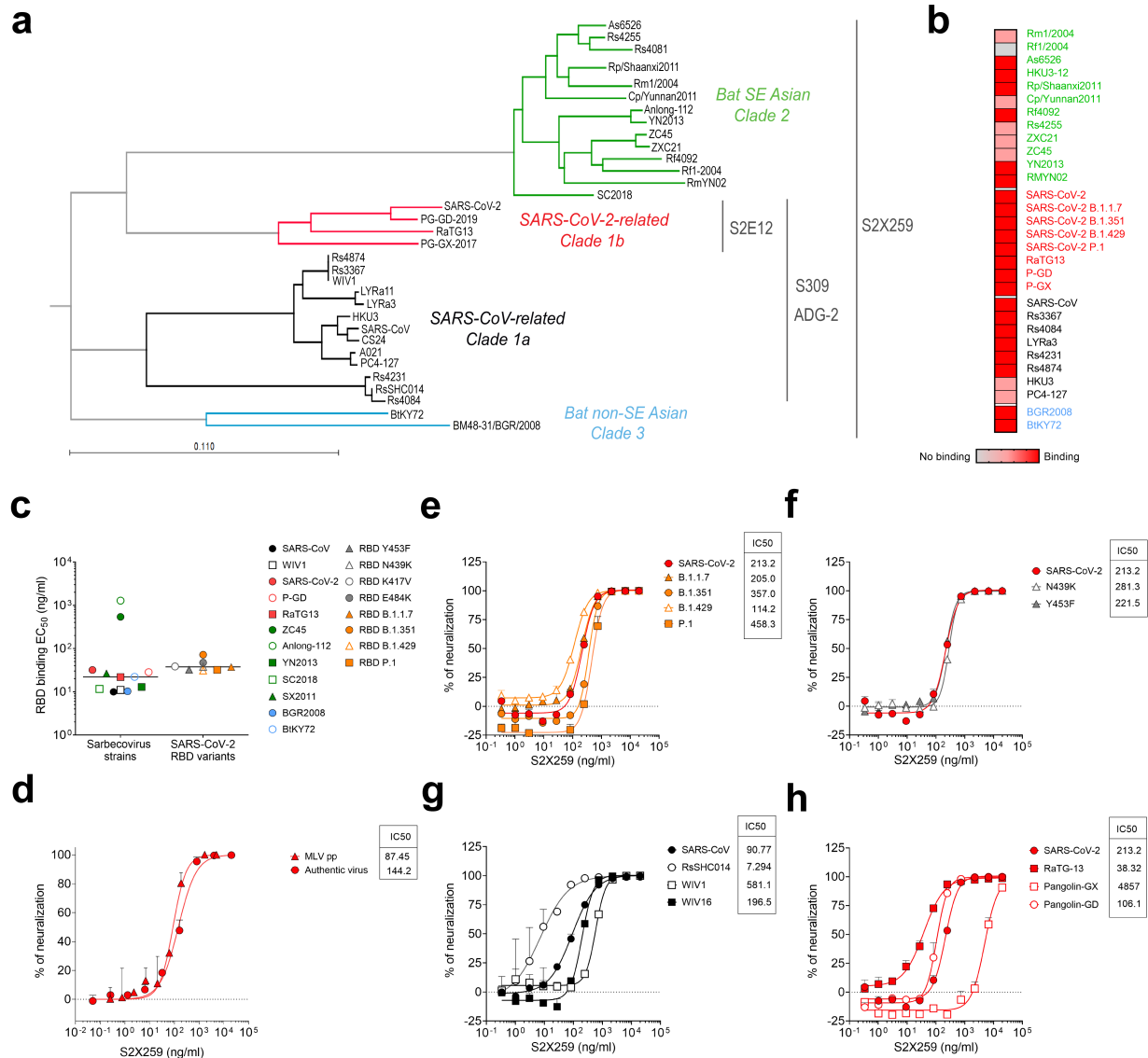


Fig. 1. Identification of a broadly neutralizing sarbecovirus mAb. **a**, Phylogenetic tree of sarbecovirus RBDs constructed via maximum likelihood analysis of amino acid sequences retrieved from GISAID and GenBank. Cross-reactivity within the sarbecovirus subgenus for S2E12⁴⁰, S309³⁰, and ADG-2²⁴ is included for comparison. **b**, Flow cytometry analysis of S2X259 cross-reactivity with a panel of 30 S glycoproteins representative of sarbecovirus clades 1a, 1b, 2, and 3 as well as SARS-CoV-2 VOCs. **c**, S2X259 binding to RBDs representative of the different sarbecovirus clades and SARS-CoV-2 variants as measured by ELISA. **d**, S2X259-mediated neutralization of SARS-CoV-2-Nluc authentic virus and SARS-CoV-2 S MLV- pseudotyped virus. **e-f** S2X259-mediated neutralization of VSV pseudotypes harbouring SARS-CoV-2 S from isolates representing the B.1.1.7, B.1.351, P.1 and B.1.429 VOC (**e**) as well as single RBD mutants (**f**). **g-h**, S2X259-mediated neutralization of VSV pseudotypes harbouring SARS-CoV-related (clade 1a, **g**) or SARS-CoV-2-related (clade 1b, **h**) S glycoproteins. One independent experiment out of at least two is shown. Error bars indicate standard deviation of duplicates or triplicates.

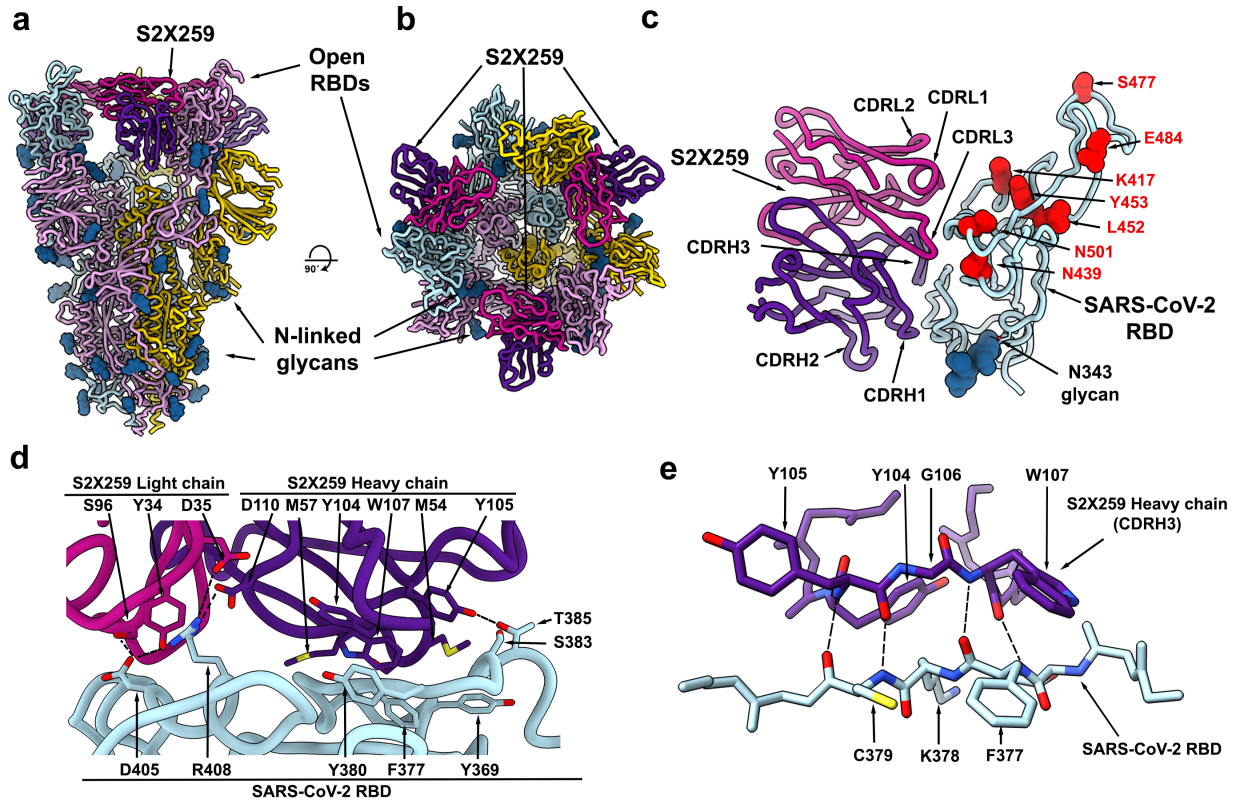


Fig. 2. The S2X259 broadly neutralizing sarbecovirus mAb recognizes RBD antigenic site II. **a-b**, CryoEM structure of the prefusion SARS-CoV-2 S ectodomain trimer with three S2X259 Fab fragments bound to three open RBDs viewed along two orthogonal orientations. **c**, The S2X259 binding pose involving contacts with multiple RBD regions. Residues corresponding to prevalent RBD mutations are shown as red spheres. **d-e**, Close-up views showing selected interactions formed between S2X259 and the SARS-CoV-2 RBD. In panels a-e, each SARS-CoV-2 S protomer is coloured distinctly (cyan, pink and gold) whereas the S2X259 light and heavy chain variable domains are coloured magenta and purple, respectively. N-linked glycans are rendered as blue spheres in panels a-c.

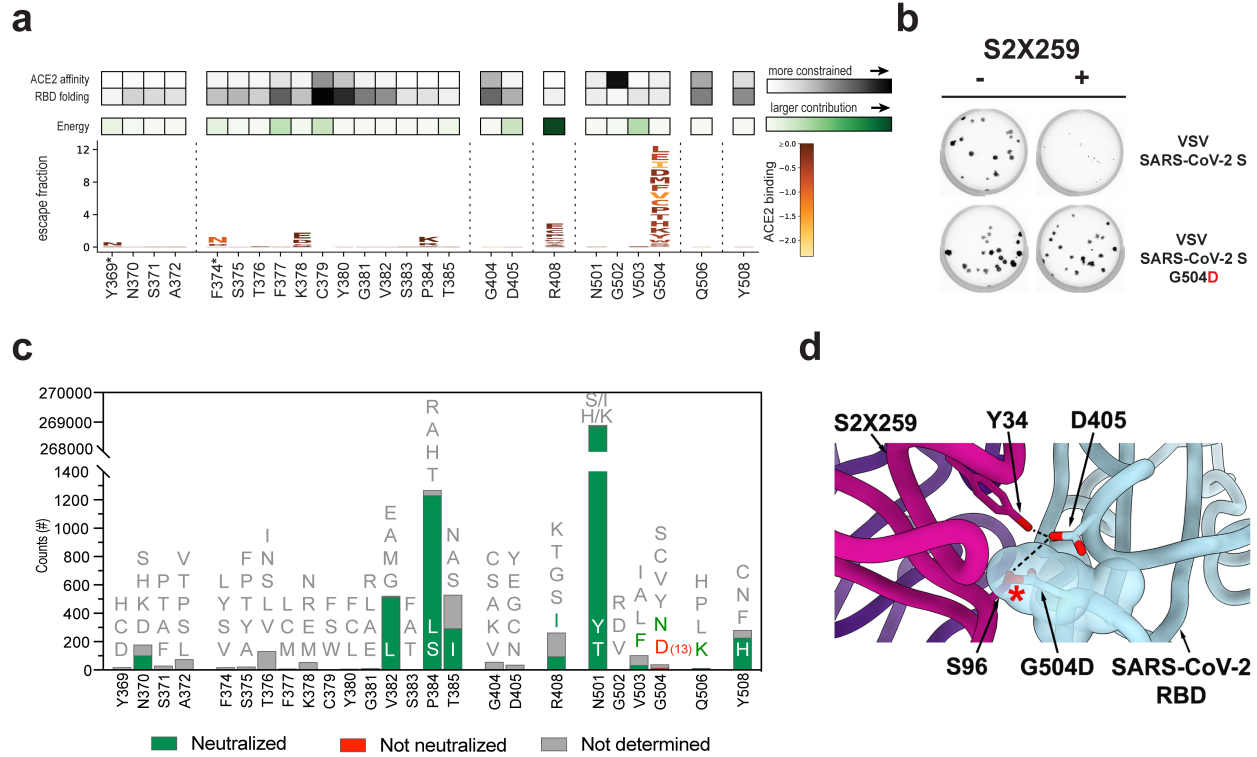


Fig. 3. S2X259 is resilient to a broad spectrum of escape mutations. **a**, Complete mapping of mutations reducing S2X259 binding using yeast-displayed RBD deep mutational scanning (DMS). Mean mutation effect on ACE2 affinity, RBD folding, and contribution to S2X259 binding for substitutions at each position in the S2X259 epitope is reported. * mutations introducing a N-linked glycosylation sites that may not be tolerated in full spike. **b**, Plaque assays performed to validate the VSV-SARS-CoV-2 G504D mutant in Vero cells in the presence (right) or absence (left) of S2X259 in the overlay. Representative image of two independent experiments is shown. **c**, Frequency of mutants at positions encompassing S2X259 epitope based on SARS-CoV-2 genome sequences available on GISAID as of April 2021. S2X259 neutralizing activity against selected mutations is reported. **d**, Zoomed-in view of the S2X259/RBD interface showing that the G504D substitution would disrupt mAb binding due to steric hindrance.

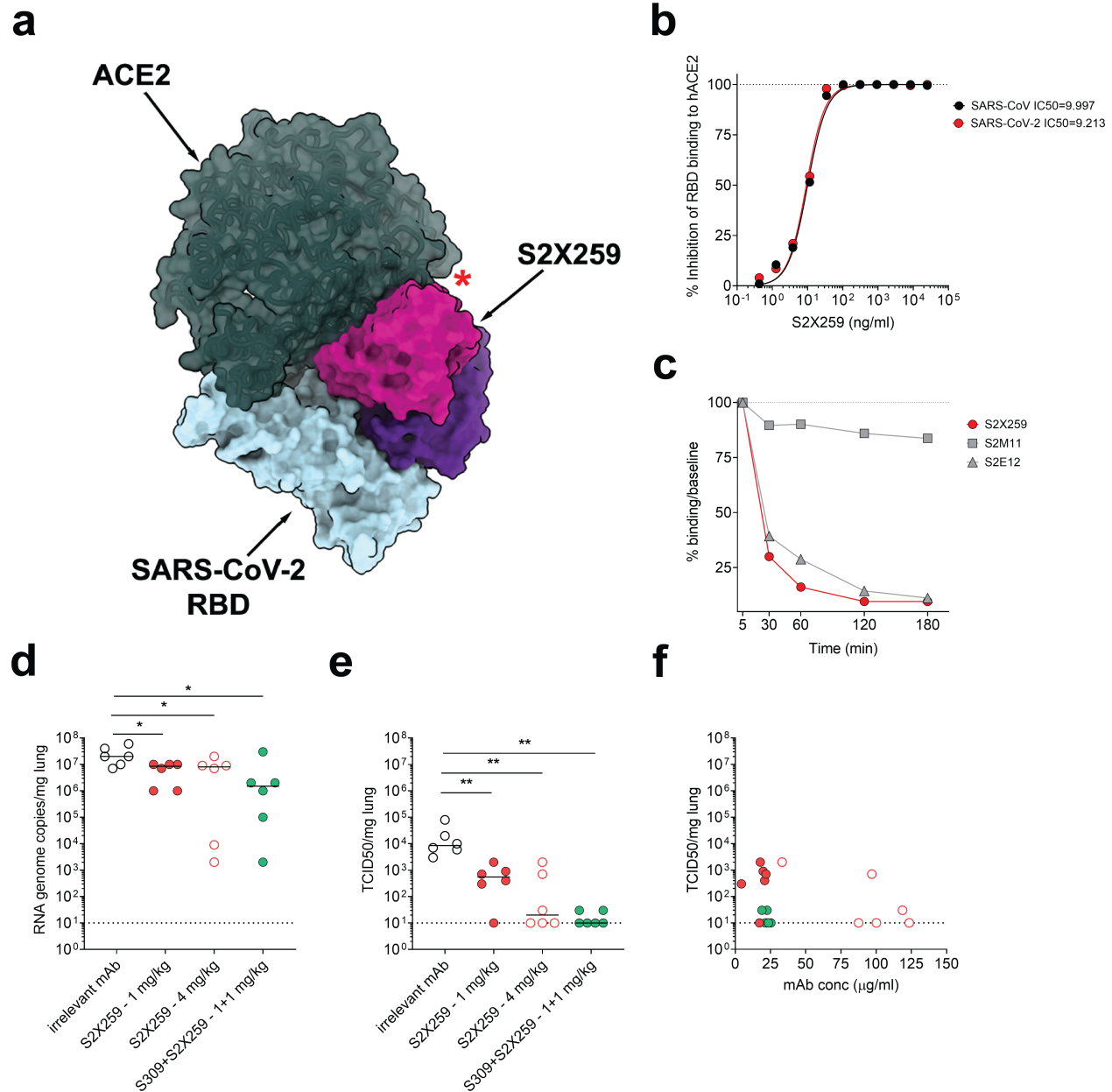
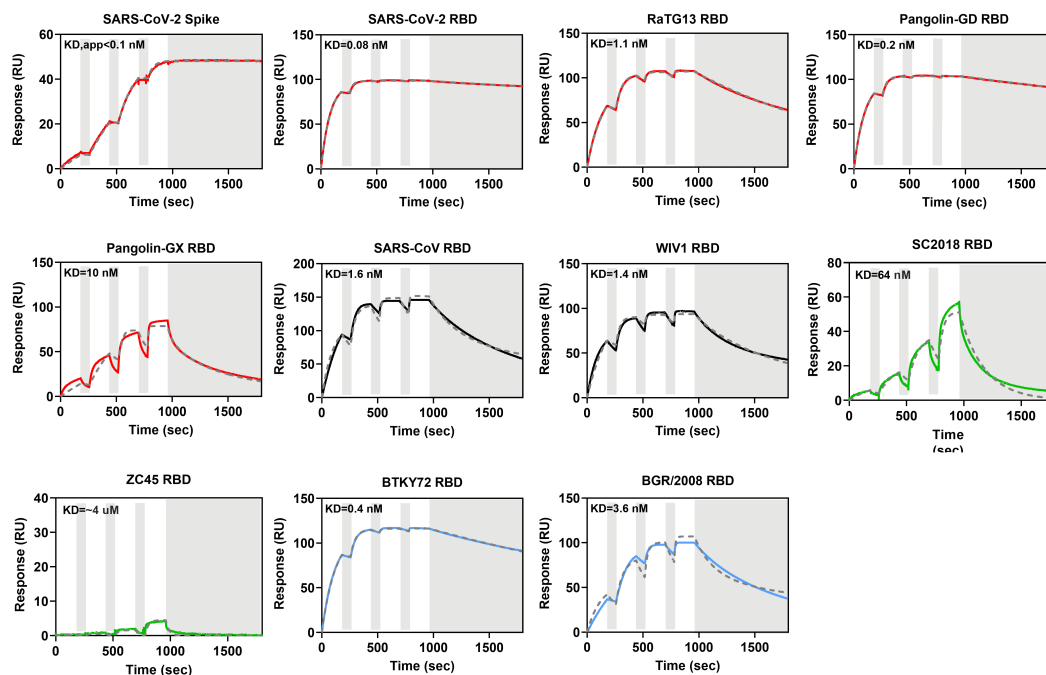
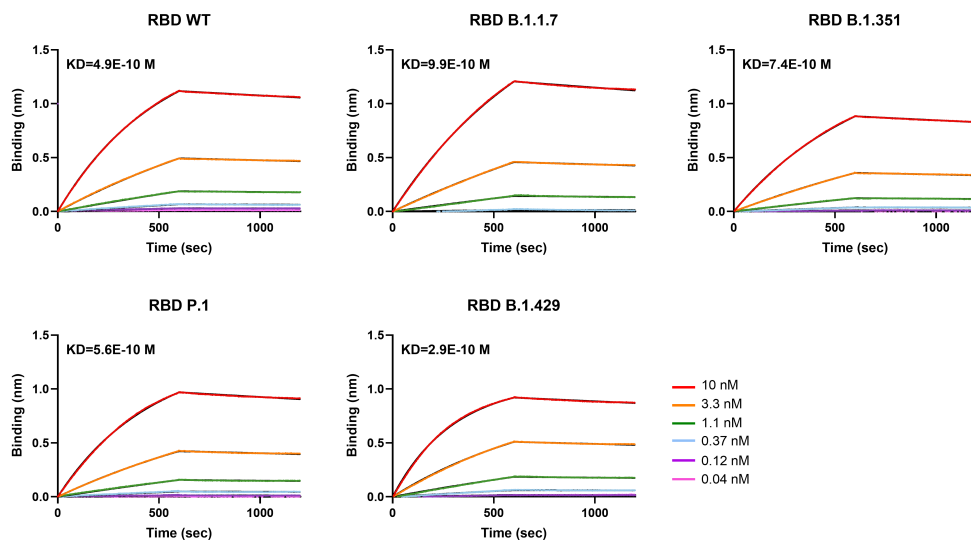


Fig. 4. S2X259 blocks ACE2 engagement, promotes shedding of the S₁ subunit and protects hamsters against B.1.351 SARS-CoV-2 challenge. **a**, S2X259 (purple/pink) and ACE2 (dark green) bind partially overlapping binding sites on the SARS-CoV-2 RBD (blue). **b**, Pre-incubation of serial dilutions of S2X259 with SARS-CoV-2 (red) or the SARS-CoV (black) RBDs prevents binding to immobilized human ACE2 (hACE2) ectodomain in ELISA. **c**, mAb-mediated S₁ subunit shedding from cell-surface expressed SARS-CoV-2 S as determined by flow-cytometry. S2E12 was included as positive control whereas S2M11 was included as negative control. **d-e**, Quantification of viral RNA loads (d) and replicating virus titres (TCID₅₀) (e) in the lungs of Syrian hamsters 4 days post intranasal challenge with B.1.351 SARS-CoV-2 VOC following prophylactic administration of S2X259 at 1 mg/kg (n=6), 4 mg/kg (n=6), and in combination with S309 (1+1 mg/kg, n=6). Mann-Whitney test was used for statistical analysis of significance. *p < 0.05, **p < 0.01. **f**, Correlation between concentration of mAbs measured in the serum before infection (day 0) infectious virus (TCID₅₀) in the lung 4 days post infection. Data from one independent experiment are presented.

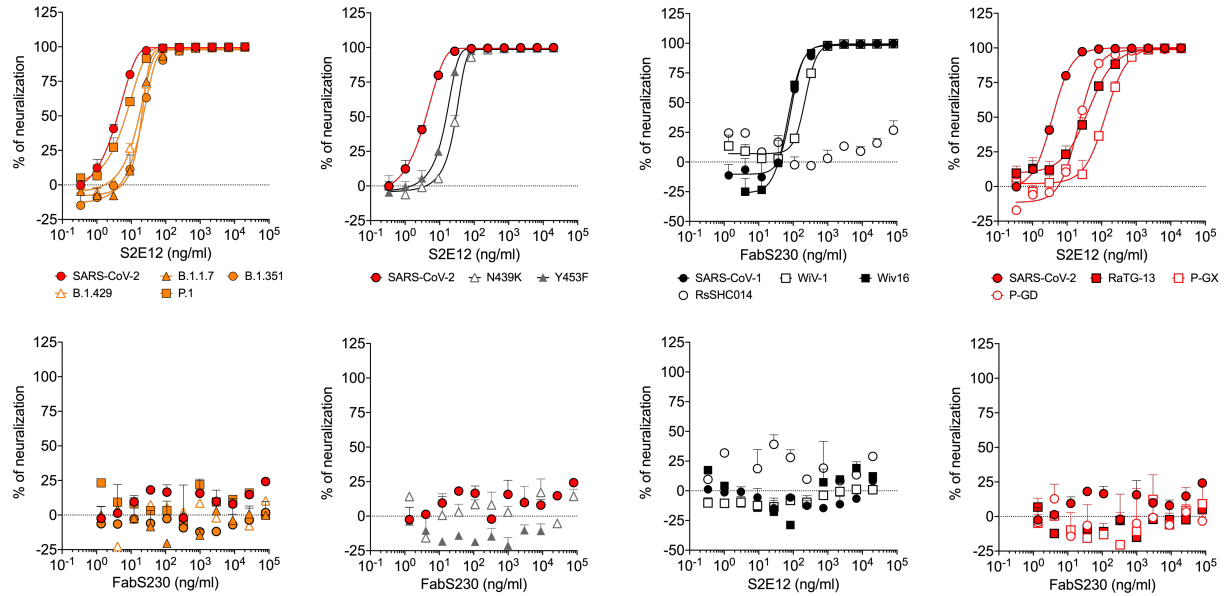
a



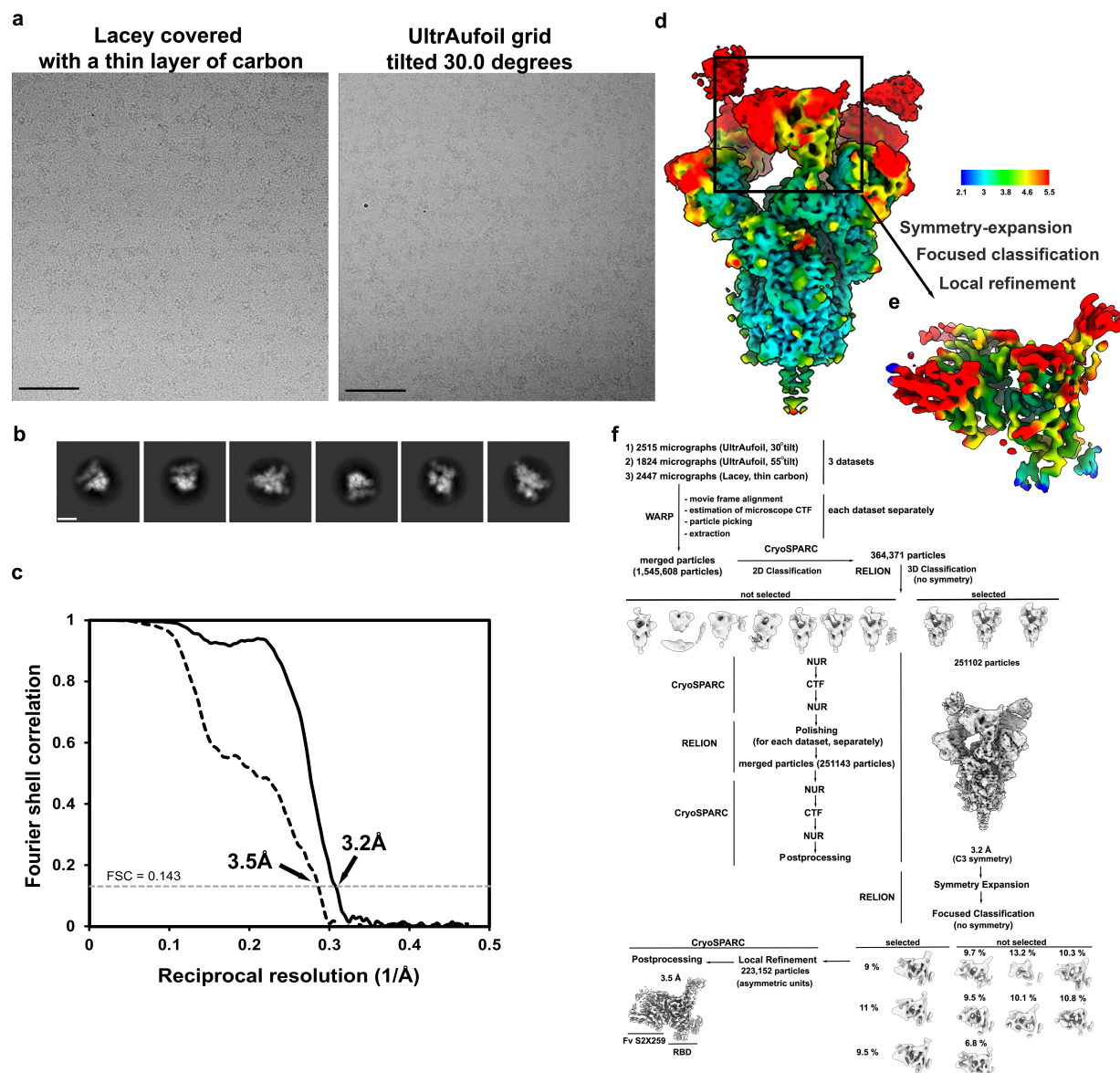
b



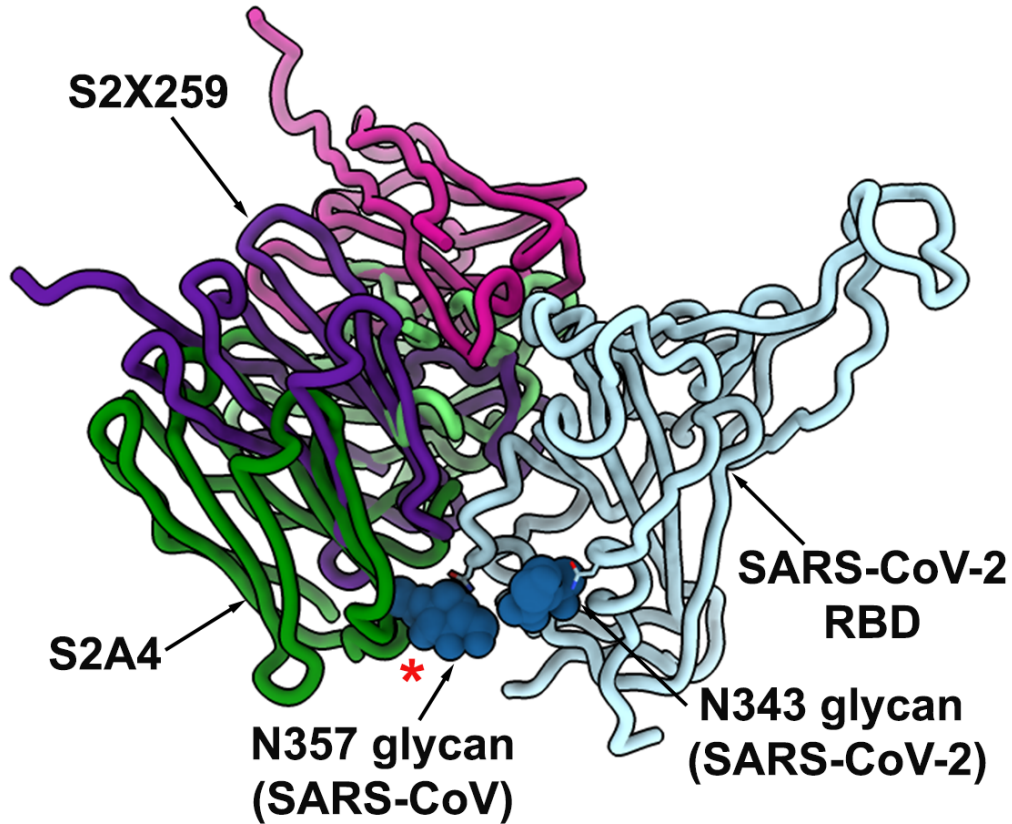
Extended Data Fig. 1. S2X259 Fab binding to recombinant sarbecovirus RBDs, prefusion SARS-CoV-2 S ectodomain trimer and RBD variants. a, S or RBD antigens were captured on the sensor chip surface and binding to S2X259 Fab at 11, 33, 100, and 300 nM was monitored successively, in single-cycle kinetics format, by surface plasmon resonance. All data have been fit to a 1:1 binding model and the equilibrium dissociation constant (K_D) is reported. For the S-binding data, we report an apparent K_D ($K_{D,app}$) since kinetics are affected by conformational dynamics between open and closed RBD states. The colouring scheme matches the phylogenetic tree in Figure 1a. **b,** Bi-layer interferometry binding analysis of the S2X259 Fab to wildtype or VOC SARS-CoV-2 biotinylated RBDs immobilized at the surface of SA biosensors.



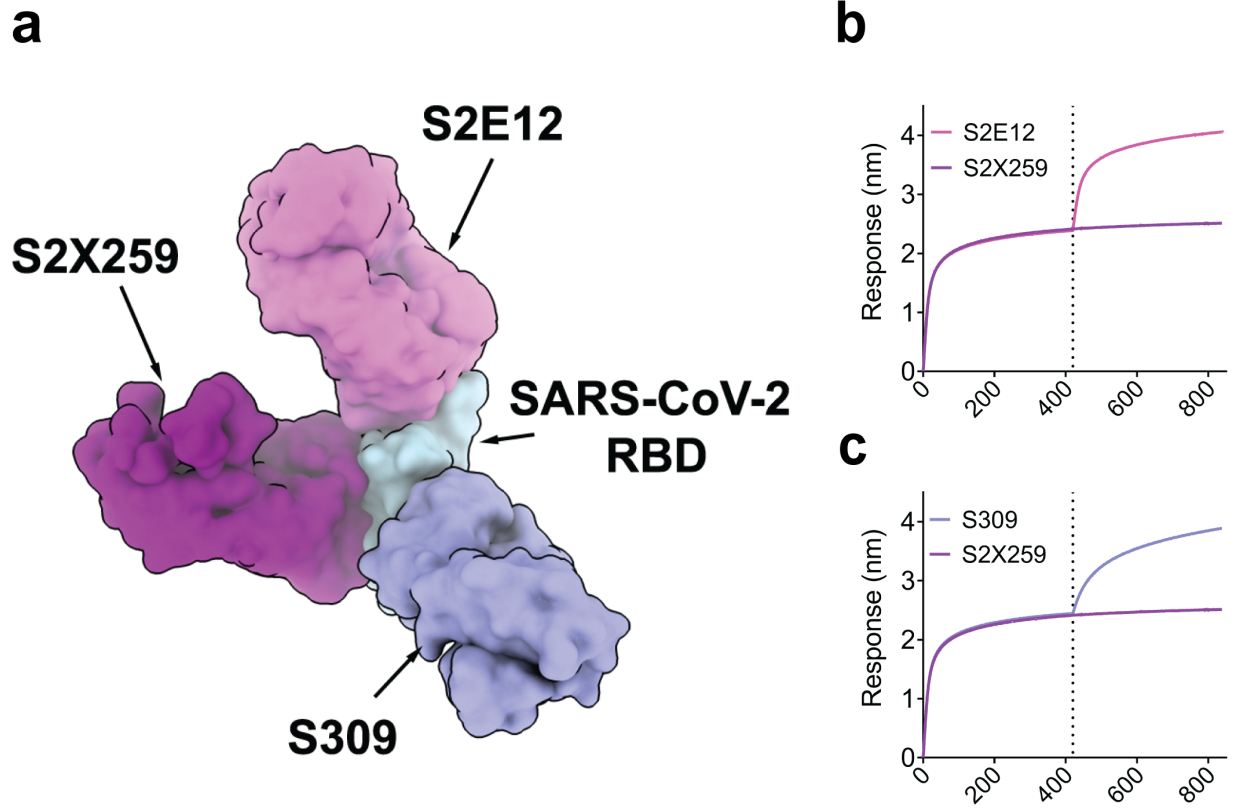
Extended Data Fig. 2. Neutralization tests with control mAbs. S2E12 and S230 neutralizing activity against VSV pseudotypes harbouring the S glycoprotein of SARS-CoV- and SARS-CoV-2 related strains and VOC.



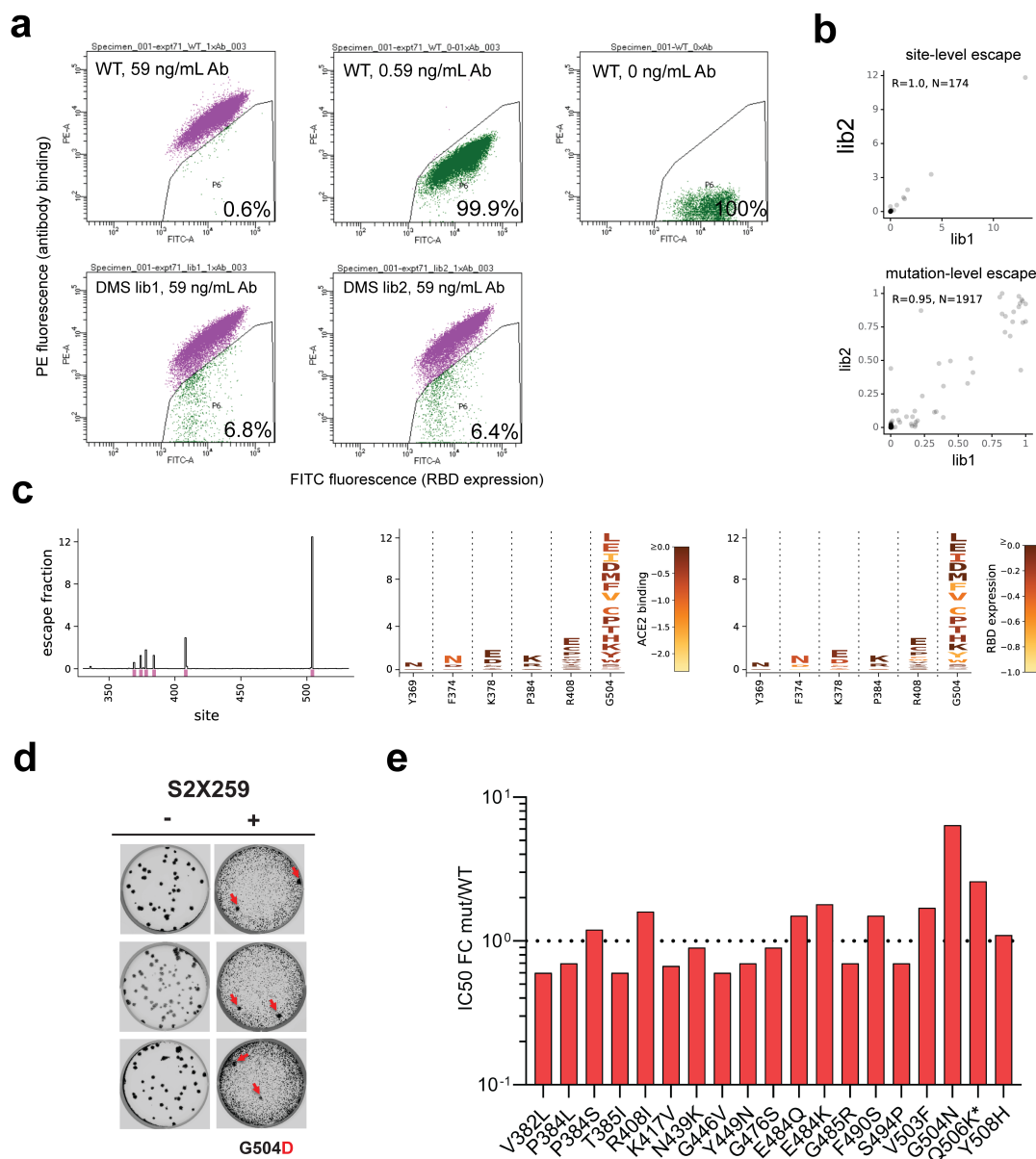
Extended Data Fig. 3. CryoEM data processing and validation of S2X259-bound SARS-CoV-2 S datasets. **a-b**, Representative electron micrographs (a) and class averages (b) of SARS-CoV-2 S in complex with the S2X259 Fab. Scale bar of the micrograph: 500 Å. Scale bar of the class averages: 100 Å. **c**, Gold-standard Fourier shell correlation curves for the S trimer bound to three S2X259 Fabs (solid black line) and the locally refined reconstruction of the RBD/S2X259 variable domains (dashed black line). The 0.143 cut-off is indicated by a horizontal dashed grey line. **d-e**, Local resolution map for the open S trimer bound to three S2X259 (d) and the locally refined reconstruction of the RBD/S2X259 variable domains (e). **f**, CryoEM data processing flow-chart.



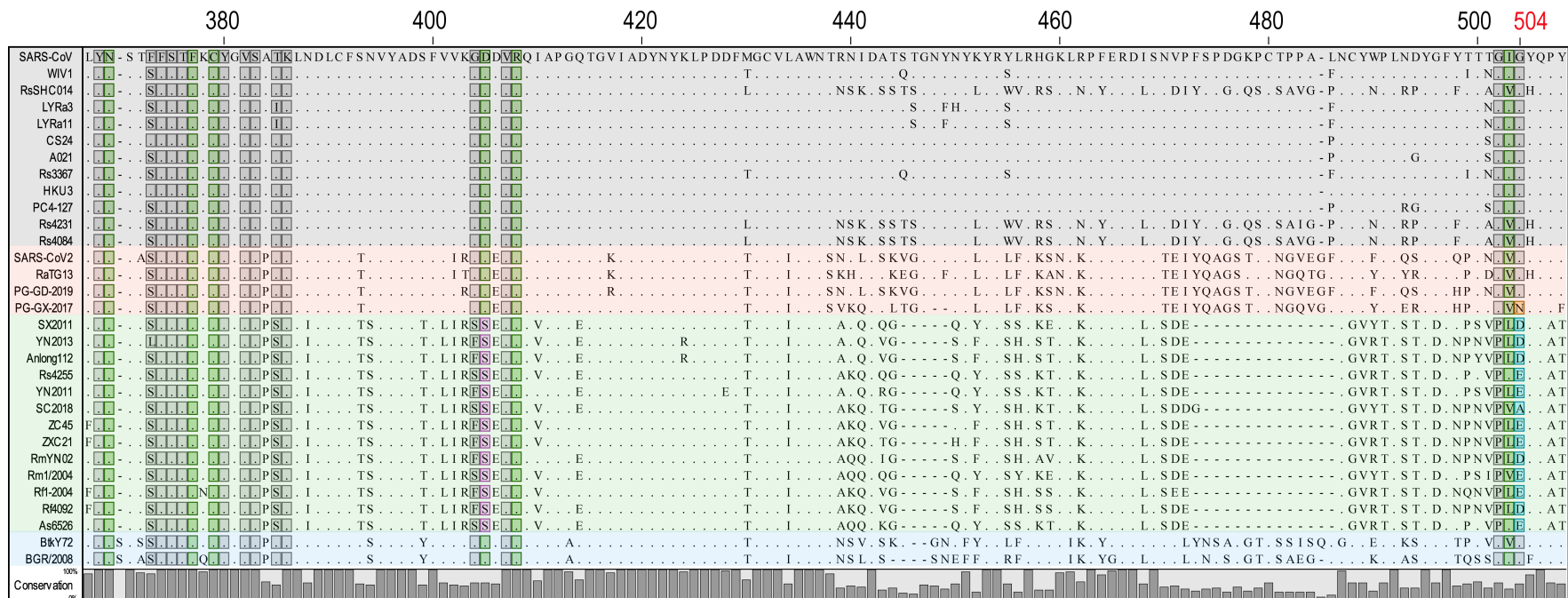
Extended Data Fig. 4. The S2X259 angle of approach for binding to the SARS-CoV-2 RBD allows to circumvent the SARS-CoV N357 glycan present in all sarbecovirus RBDs except SARS-CoV-2. Ribbon diagram showing a superimposition of the S2X259-bound and S2A4-bound (PDB 7JVA) SARS-CoV-2 RBD²¹. The SARS-CoV glycan at position N357 was modelled based on the S230-bound SARS-CoV S structure (PDB 6NB6³⁷) and is predicted to sterically hinder S2A4 binding (red star) but not S2X259. The mAb light and heavy chains are coloured magenta and purple (S2X259) or light and dark green (S2A4). N-linked glycans are rendered as blue spheres.



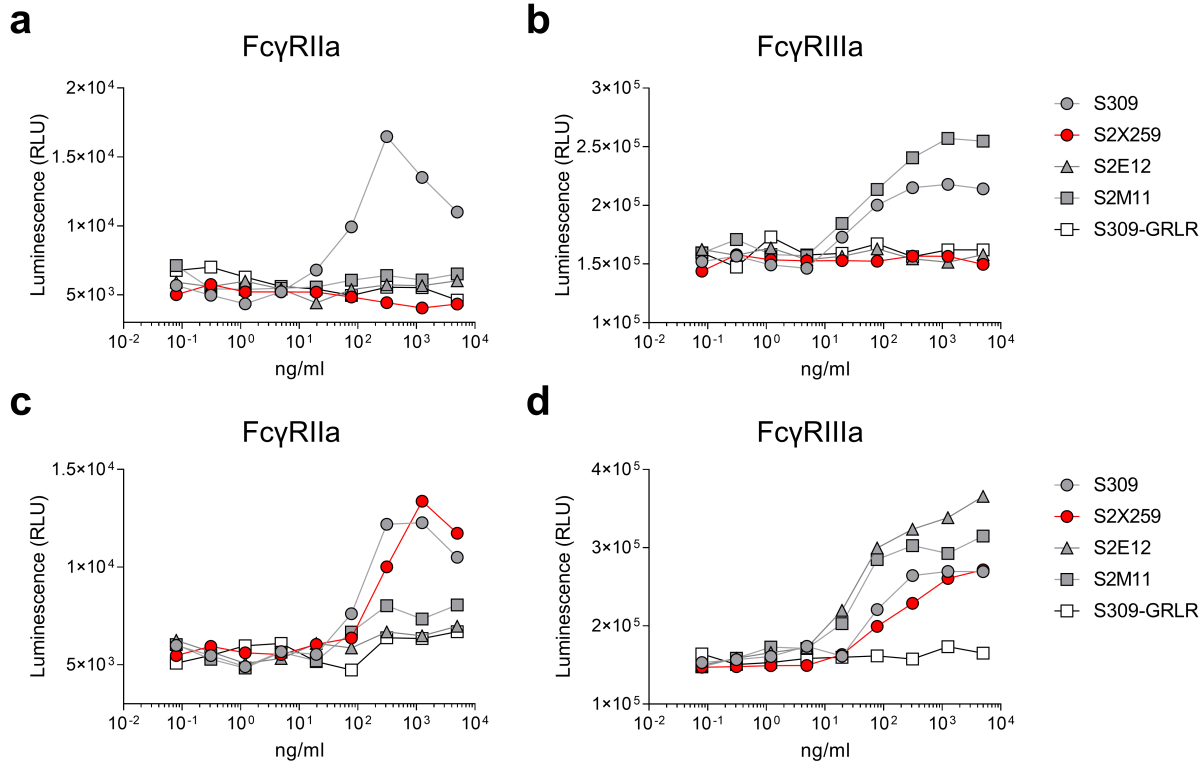
Extended Data Fig. 5. S2X259 allows combination with site I and IV-targeting mAbs. **a**, View of site I-targeting S2E12⁴⁰ (pink), site II-targeting S2X259 (magenta), and site IV-targeting S309³⁰ (purple) mAb binding to SARS-CoV-2 RBD (light blue). **b-c**, Competition binding assays for S2X259 vs site I-targeting S2E12 (b) and site IV-targeting S309 (c) mAbs on SARS-CoV-2 RBD as measured by biolayer interferometry. One independent experiment out of two is shown.



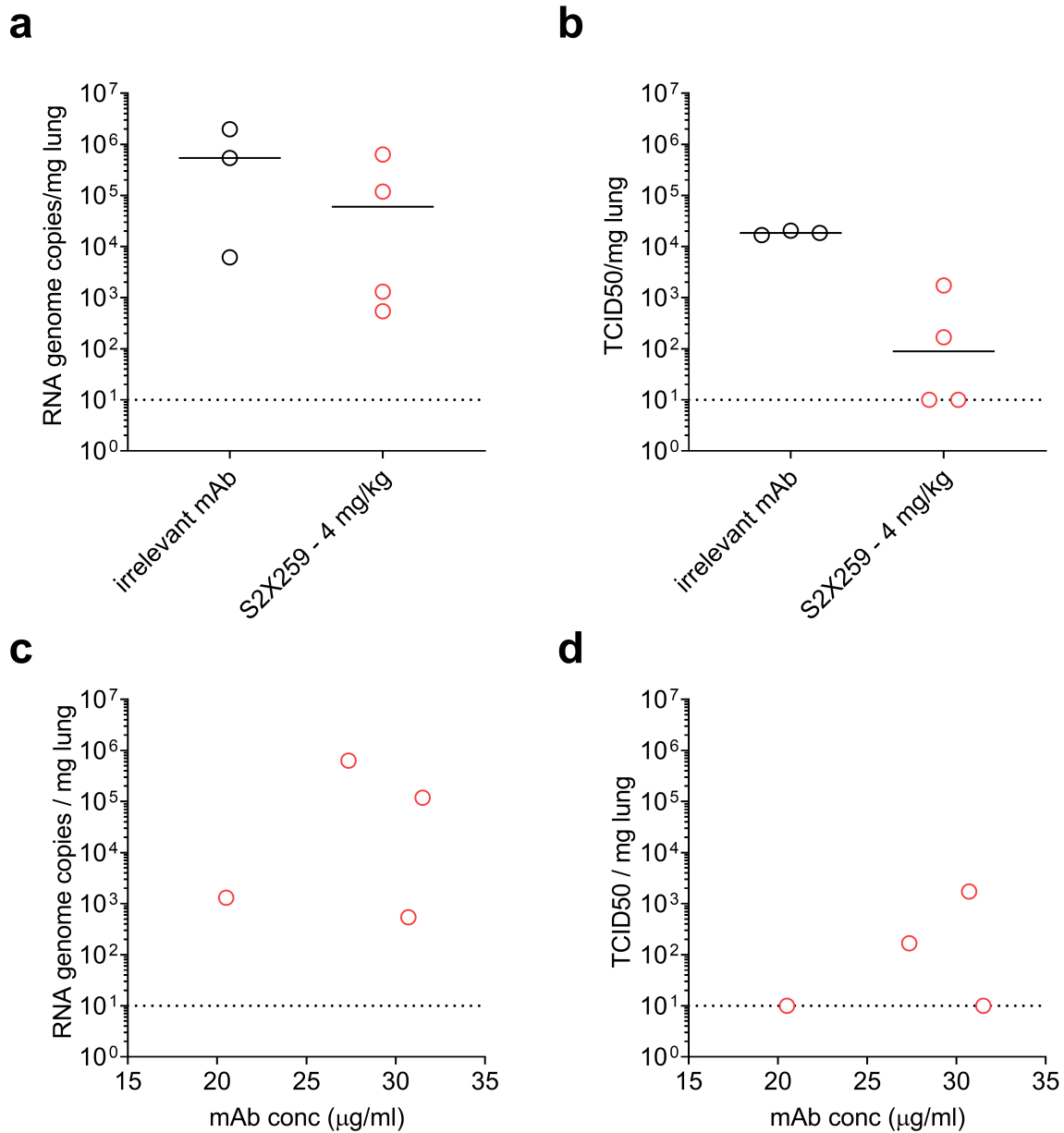
Extended Data Fig. 6. S2X259 has a high barrier for the emergence of resistance mutants. **a**, FACS gates used in DMS to select escape variants. Top row: yeast controls expressing unmutated SARS-CoV-2 RBD labelled at relevant S2X259 concentrations for setting of selection gates. Bottom row: fraction of cells in SARS-CoV-2 mutant libraries falling into the antibody-escape bin. **b**, Correlation in site-level (top, sum of escape fractions for mutations at a site) and mutation-level (bottom) escape between independently generated and assayed RBD mutant libraries. **c**, Line plot of escape mutants along all positions in the SARS-CoV-2 RBD (left). Pink lines indicate sites that escape S2X259 binding illustrated at the mutation-level in logoplots (right). In logoplots, the height of a letter scales with its escape fraction. Letters are coloured according to their deleterious consequences for ACE2 binding (middle) or RBD expression (right) as determined in prior deep mutational scanning experiments³³. **d**, Plaque assay on Vero cells with no antibody (left) or S2X259 (right) in the overlay to isolate escape mutants (red arrow). Data are representative of three independent experiments. **e**, S2X259 in vitro neutralizing activity against SARS-CoV-2 S VSV pseudotyped mutants. For each mutant the fold change of the IC₅₀ geometric mean vs SARS-CoV-2 S WT is reported. *Q506K displayed a 10-fold reduction in viral entry in comparison to the other mutants. Results from two independent experiments are reported.



Extended Data Fig. 7. S2X259 epitope conservation across sarbecovirus clades. Protein sequence alignment of representative sarbecovirus RBDs with strictly conserved residues shown as dots. Overall conservation is represented as a bar plot. Positions are based on SARS-CoV-2 RBD. Residues determined to be important for S2X259 binding are denoted in dark green. Substitutions at positions D405 and G504 are indicated in pink and blue/orange, respectively. Additional residues representing extended epitope, are denoted grey. Different clades within the sarbecovirus subgenus are overlaid in grey (clade 1a), red (clade 1b), green (clade 2), and light blue (clade 3).



Extended Data Fig. 8. S2X259 Fc-mediated activation of FcγRIIa and FcγRIIIa *in vitro*. a-b, NFAT-driven luciferase signal induced in Jurkat cells stably expressing FcγRIIa H131 (a) variant or FcγRIIIa V158 (b) variant by S2X259 binding to full-length wild-type SARS-CoV-2 S on ExpiCHO target cells. c-d, NFAT-driven luciferase signal induced in Jurkat cells stably expressing FcγRIIa H131 (c) or FcγRIIIa V158 (d) variants by S2X259 binding to uncleavable full-length pre-fusion stabilized SARS-CoV-2 S (unable to release the S₁ subunit) transiently expressed in ExpiCHO cells. SE12, S2M11, S309, S309-GRLR mAbs are included as controls.



Extended Data Fig. 9. Prophylactic administration of S2X259 mAb protects hamsters against prototypic (Wuhan-1 related) SARS-CoV-2 challenge. a-b, Viral RNA loads (a) and replicating virus titres (b) in the lungs of Syrian hamsters 4 days post-intranasal infection with prototypic SARS-CoV-2. Results for one independent experiment are shown. c-d, Viral RNA loads and replicating virus titers in the lung 4 days post infection plotted as a function of serum mAb concentrations before infection (day 0). Irrelevant mAb n=3; S2X259 4 mg/kg n=4.

SUPPLEMENTARY TABLES

Table S1. Characteristics of S2X259. VH and VL % identity refers to V gene identity compared to germline (IMGT).

Donor Gender	Male
Donor Age	52
Donor Status	Symptomatic
Days after symptoms onset	75
VH gene usage	VH1-69
VH % identity	94.1
HCDR3	ARGFNGNYYGWGDDDAFDI
VL gene usage	VL1-40
VL % identity	98.26
LCDR3	QSYDSSLGPNWV

Table S2. CryoEM data collection and refinement statistics.

	SARS-CoV-2 S/S2X259	SARS-CoV-2 S/S2X259 (local refinement)
Data collection and processing		
Magnification	130,000	130,000
Voltage	300	300
Electron exposure (e ⁻ /Å ²)		
Defocus range (μm)	0.8-2.0	0.8-2.0
Pixel size (Å)	0.525	0.525
Symmetry imposed	C3	C1
Final particle images (no.)		
Map resolution (Å)	3.2	3.5
FSC threshold	0.143	0.143
Validation		
MolProbity score	1.08	0.74
Clash score	1.7	0.16
Poor rotamers (%)	0.38	5.29
Ramachandran plot		
Favored (%)	97.1	97.01
Allowed (%)	2.9	2.74
Disallowed (%)	-	0.25

Table S3. X-ray data collection and refinement statistics.

	RBD/S2X259/S2H97 PDB ID: 7M7W
Data collection	
Space group	P2 ₁
Cell dimensions	
<i>a</i> , <i>b</i> , <i>c</i> (Å)	86.19, 66.40, 237.66
α , β , γ (°)	90.00, 94.34, 90.00
Resolution (Å)	63.94-2.65 (2.70-2.65)
<i>R</i> _{merge}	0.149 (2.494)
<i>I</i> / σI	10.9 (0.8)
Completeness (%)	98.6 (98.3)
Redundancy	6.9 (6.8)
Refinement	
Resolution (Å)	2.65
No. reflections	73,189
<i>R</i> _{work} / <i>R</i> _{free}	0.221/0.271
No. atoms	
Protein	16,162
Ligand/ion	28
Water	95
<i>B</i> -factors	
Protein	75.86
Ligand	84.00
Water	50.09
R.m.s. deviations	
Bond lengths (Å)	0.002
Bond angles (°)	0.817

Values for the highest-resolution shell are shown in parentheses.

Table S4. Summary of nucleotide and amino acid mutations found in 18 neutralization-resistant VSV-SARS-CoV-2-S chimera plaques.

Plaque	Nucleotide mutant	Amino acid Mutant
1	G1511A	G504D
2	G1511A	G504D
3	G1511A	G504D
4	G1511A	G504D
5	G1511A	G504D
6	G1511A	G504D
7	G1511A	G504D
8	G1511A	G504D
9	G1511A	G504D
10	G1511A	G504D
11	G1511A	G504D
12	G1511A	G504D
13	G1511A	G504D
14	G1511A	G504D
15	G1511A	G504D
16	G1511A	G504D
17	G1511A	G504D
18	G1511A	G504D

REFERENCES

1. Zhou, P. *et al.* A pneumonia outbreak associated with a new coronavirus of probable bat origin. *Nature* **579**, 270-273 (2020).
2. Kuiken, T. *et al.* Newly discovered coronavirus as the primary cause of severe acute respiratory syndrome. *Lancet* **362**, 263-270 (2003).
3. Deng, Xianding *et al.* Transmission, infectivity, and antibody neutralization of an emerging SARS-CoV-2 variant in California carrying a L452R spike protein mutation. *medRxiv*: <https://doi.org/10.1101/2021.03.07.21252647> (2021).
4. Challen, R. *et al.* Risk of mortality in patients infected with SARS-CoV-2 variant of concern 202012/1: matched cohort study. *BMJ* **372**, n579 (2021).
5. Davies, N. G. *et al.* Estimated transmissibility and impact of SARS-CoV-2 lineage B.1.1.7 in England. *Science* doi: 10.1126/science.abg3055 (2021).
6. Tegally, H. *et al.* Emergence of a SARS-CoV-2 variant of concern with mutations in spike glycoprotein. *Nature*, doi:10.1038/s41586-021-03402-9 (2021).
7. Wang, Z. *et al.* mRNA vaccine-elicited antibodies to SARS-CoV-2 and circulating variants. *Nature*, doi:10.1038/s41586-021-03324-6 (2021).
8. Collier, D. A. *et al.* SARS-CoV-2 B.1.1.7 sensitivity to mRNA vaccine-elicited, convalescent and monoclonal antibodies. *medRxiv*, doi:10.1038/s41586-021-03412-7 (2021).
9. S Arunachalam, P. *et al.* Adjuvanting a subunit SARS-CoV-2 nanoparticle vaccine to induce protective immunity in non-human primates. *bioRxiv*, doi:10.1101/2021.02.10.430696 (2021).
10. Wu, K. *et al.* Serum Neutralizing Activity Elicited by mRNA-1273 Vaccine - Preliminary Report. *N. Engl. J. Med.*, doi:10.1056/NEJMc2102179 (2021).
11. Ho, D. *et al.* Increased Resistance of SARS-CoV-2 Variants B.1.351 and B.1.1.7 to Antibody Neutralization. *Res. Sq*, doi: 10.21203/rs.3.rs-155394/v1 (2021).
12. Wibmer, C. K. *et al.* SARS-CoV-2 501Y.V2 escapes neutralization by South African COVID-19 donor plasma. *Nat. Med.*, doi:10.1038/s41591-021-01285-x (2021).
13. Wang, P. *et al.* Increased Resistance of SARS-CoV-2 Variants B.1.351 and B.1.1.7 to Antibody Neutralization. *bioRxiv*, doi:10.1101/2021.01.25.428137 (2021).
14. Chen, R. E. *et al.* Resistance of SARS-CoV-2 variants to neutralization by monoclonal and serum-derived polyclonal antibodies. *Nat. Med.*, doi:10.1038/s41591-021-01294-w (2021).
15. Madhi, S. A. *et al.* Efficacy of the ChAdOx1 nCoV-19 Covid-19 Vaccine against the B.1.351 Variant. *N. Engl. J. Med.*, doi:10.1056/NEJMoa2102214 (2021).
16. Walls, A. C. *et al.* Structure, Function, and Antigenicity of the SARS-CoV-2 Spike Glycoprotein. *Cell* **181**, 281-292.e6 (2020).
17. Wrapp, D. *et al.* Cryo-EM structure of the 2019-nCoV spike in the prefusion conformation. *Science* **367**, 1260-1263 (2020).
18. Kuhn, J. H., Li, W., Choe, H. & Farzan, M. Angiotensin-converting enzyme 2: a functional receptor for SARS coronavirus. *Cell Mol. Life Sci.* **61**, 2738-2743 (2004).

19. Hoffmann, M. *et al.* SARS-CoV-2 Cell Entry Depends on ACE2 and TMPRSS2 and Is Blocked by a Clinically Proven Protease Inhibitor. *Cell* **181**, 271-280.e8 (2020).
20. Letko, M., Marzi, A. & Munster, V. Functional assessment of cell entry and receptor usage for SARS-CoV-2 and other lineage B betacoronaviruses. *Nat. Microbiol.* **5**, 562-569 (2020).
21. Piccoli, L. *et al.* Mapping Neutralizing and Immunodominant Sites on the SARS-CoV-2 Spike Receptor-Binding Domain by Structure-Guided High-Resolution Serology. *Cell* **183**, 1024-1042.e21 (2020).
22. Cohen, A. A. *et al.* Mosaic nanoparticles elicit cross-reactive immune responses to zoonotic coronaviruses in mice. *Science* **371**, 735-741 (2021).
23. Yuan, M. *et al.* A highly conserved cryptic epitope in the receptor binding domains of SARS-CoV-2 and SARS-CoV. *Science* **368**, 630-633 (2020).
24. Rappazzo, C. G. *et al.* Broad and potent activity against SARS-like viruses by an engineered human monoclonal antibody. *Science* **371**, 823-829 (2021).
25. Davies, N. G. *et al.* Increased hazard of death in community-tested cases of SARS-CoV-2 Variant of Concern 202012/01. *medRxiv*, doi:10.1101/2021.02.01.21250959 (2021).
26. Thomson, E. C. *et al.* Circulating SARS-CoV-2 spike N439K variants maintain fitness while evading antibody-mediated immunity. *Cell* **184**, 1171-1187 (2021).
27. Nuno R. Faria *et al.* Genomic characterisation of an emergent SARS-CoV-2 lineage in Manaus: preliminary findings. <https://virological.org/t/genomic-characterisation-of-an-emergent-sars-cov-2-lineage-in-manaus-preliminary-findings/586>. (2021).
28. Starr T.N. *et al.* Antibodies to the SARS-CoV-2 receptor-binding domain that maximize breadth and resistance to viral escape. *Nature - manuscript submitted*.
29. Barnes, C. O. *et al.* SARS-CoV-2 neutralizing antibody structures inform therapeutic strategies. *Nature* **588**, 682-687 (2020).
30. Pinto, D. *et al.* Cross-neutralization of SARS-CoV-2 by a human monoclonal SARS-CoV antibody. *Nature* **583**, 290-295 (2020).
31. Cathcart, A.,L. *et al.* The dual function monoclonal antibodies VIR-7831 and VIR-7832 demonstrate potent in vitro and in vivo activity against SARS-CoV-2. *bioRxiv*, doi: <https://doi.org/10.1101/2021.03.09.434607> (2021).
32. Greaney, A. J. *et al.* Complete Mapping of Mutations to the SARS-CoV-2 Spike Receptor-Binding Domain that Escape Antibody Recognition. *Cell. Host Microbe* **29**, 44-57.e9 (2021).
33. Starr, T. N. *et al.* Deep Mutational Scanning of SARS-CoV-2 Receptor Binding Domain Reveals Constraints on Folding and ACE2 Binding. *Cell* **182**, 1295-1310.e20 (2020).
34. Case, J. B. *et al.* Replication-Competent Vesicular Stomatitis Virus Vaccine Vector Protects against SARS-CoV-2-Mediated Pathogenesis in Mice. *Cell. Host Microbe* **28**, 465-474.e4 (2020).
35. Liu, Z. *et al.* Identification of SARS-CoV-2 spike mutations that attenuate monoclonal and serum antibody neutralization. *Cell. Host Microbe* **29**, 477-478.e4 (2021).
36. Huo, J. *et al.* Neutralization of SARS-CoV-2 by Destruction of the Prefusion Spike. *Cell. Host Microbe* **28**, 445-454.e6 (2020).

37. Walls, A. C. *et al.* Unexpected Receptor Functional Mimicry Elucidates Activation of Coronavirus Fusion. *Cell* **176**, 1026-1039.e15 (2019).
38. Wec, A. Z. *et al.* Broad neutralization of SARS-related viruses by human monoclonal antibodies. *Science* **369**, 731-736 (2020).
39. Wrobel, A. G. *et al.* Antibody-mediated disruption of the SARS-CoV-2 spike glycoprotein. *Nat. Commun.* **11**, 5337-020-19146-5 (2020).
40. Tortorici, M. A. *et al.* Ultrapotent human antibodies protect against SARS-CoV-2 challenge via multiple mechanisms. *Science* **370**, 950-957 (2020).
41. Boudewijns, R. *et al.* STAT2 signaling restricts viral dissemination but drives severe pneumonia in SARS-CoV-2 infected hamsters. *Nat. Commun.* **11**, 5838-020-19684-y (2020).
42. Schäfer, A. *et al.* Antibody potency, effector function, and combinations in protection and therapy for SARS-CoV-2 infection in vivo. *J. Exp. Med.* **218**, e20201993. doi: 10.1084/jem.20201993 (2021).
43. Winkler, E. S. *et al.* Human neutralizing antibodies against SARS-CoV-2 require intact Fc effector functions and monocytes for optimal therapeutic protection. *Cell* **184**, 1804-1820 (2021).
44. Abdelnabi, Rana *et al.* Comparative infectivity and pathogenesis of emerging SARS-CoV-2 variants in Syrian hamsters. *bioRxiv*, doi: <https://doi.org/10.1101/2021.02.26.433062> (2021).
45. Walls, A.,C. *et al.* Elicitation of broadly protective sarbecovirus immunity by receptor-binding domain nanoparticle vaccines. *bioRxiv*: doi: <https://doi.org/10.1101/2021.03.15.435528> (2021).
46. Menachery, V. D. *et al.* A SARS-like cluster of circulating bat coronaviruses shows potential for human emergence. *Nat. Med.* **21**, 1508-1513 (2015).
47. Menachery, V. D. *et al.* SARS-like WIV1-CoV poised for human emergence. *Proc. Natl. Acad. Sci. U. S. A.* **113**, 3048-3053 (2016).
48. Yang, X. L. *et al.* Isolation and Characterization of a Novel Bat Coronavirus Closely Related to the Direct Progenitor of Severe Acute Respiratory Syndrome Coronavirus. *J. Virol.* **90**, 3253-3256 (2015).
49. Ge, X. Y. *et al.* Isolation and characterization of a bat SARS-like coronavirus that uses the ACE2 receptor. *Nature* **503**, 535-538 (2013).
50. Martinez, D.,R. *et al.* Chimeric spike mRNA vaccines protect against sarbecovirus challenge in mice. *bioRxiv*, doi: <https://doi.org/10.1101/2021.03.11.434872> (2021).
51. Makarenkov, V., Mazouze, B., Rabusseau, G. & Legendre, P. Horizontal gene transfer and recombination analysis of SARS-CoV-2 genes helps discover its close relatives and shed light on its origin. *BMC Ecol. Evol.* **21**, 5-020-01732-2 (2021).
52. Greaney, A. J. *et al.* Comprehensive mapping of mutations in the SARS-CoV-2 receptor-binding domain that affect recognition by polyclonal human plasma antibodies. *Cell. Host Microbe* **29**, 463-476.e6 (2021).
53. Walls, A. C. *et al.* Elicitation of Potent Neutralizing Antibody Responses by Designed Protein Nanoparticle Vaccines for SARS-CoV-2. *Cell* **183**, 1367-1382.e17 (2020).

54. Slater, G. S., C. & Birney, E. Automated generation of heuristics for biological sequence comparison. *BMC Bioinformatics* **6**, 31 (2005).
55. Katoh, K. & Standley, D. M. MAFFT multiple sequence alignment software version 7: improvements in performance and usability. *Mol. Biol. Evol.* **30**, 772-780 (2013).
56. Ou, X. *et al.* Characterization of spike glycoprotein of SARS-CoV-2 on virus entry and its immune cross-reactivity with SARS-CoV. *Nat. Commun.* **11**, 1620-020-15562-9 (2020).
57. Crawford, K. H. D. *et al.* Protocol and Reagents for Pseudotyping Lentiviral Particles with SARS-CoV-2 Spike Protein for Neutralization Assays. *Viruses* **12**, 513. doi: 10.3390/v12050513 (2020).
58. Xie, X. *et al.* A nanoluciferase SARS-CoV-2 for rapid neutralization testing and screening of anti-infective drugs for COVID-19. *Nat. Commun.* **11**, 5214-020-19055-7 (2020).
59. Reed, L. J. & Muench, H. A simple method of estimating fifty per cent endpoints. *Am. J. Epidemiol.* **27**, 493-497 (1938).
60. Starr, T. N. *et al.* Prospective mapping of viral mutations that escape antibodies used to treat COVID-19. *Science* **371**, 850-854 (2021).
61. Kabsch, W. Xds. *Acta Crystallogr. D Biol. Crystallogr.* **66**, 125-132 (2010).
62. McCoy, A. J. *et al.* Phaser crystallographic software. *J. Appl. Crystallogr.* **40**, 658-674 (2007).
63. Emsley, P., Lohkamp, B., Scott, W. G. & Cowtan, K. Features and development of Coot. *Acta Crystallogr. D Biol. Crystallogr.* **66**, 486-501 (2010).
64. Croll, T. I. ISOLDE: a physically realistic environment for model building into low-resolution electron-density maps. *Acta Crystallogr. D. Struct. Biol.* **74**, 519-530 (2018).
65. Murshudov, G. N. *et al.* REFMAC5 for the refinement of macromolecular crystal structures. *Acta Crystallogr. D Biol. Crystallogr.* **67**, 355-367 (2011).
66. Suloway, C. *et al.* Automated molecular microscopy: the new Legion system. *J. Struct. Biol.* **151**, 41-60 (2005).
67. Tegunov, D. & Cramer, P. Real-time cryo-electron microscopy data preprocessing with Warp. *Nat. Methods* **16**, 1146-1152 (2019).
68. Punjani, A., Rubinstein, J. L., Fleet, D. J. & Brubaker, M. A. cryoSPARC: algorithms for rapid unsupervised cryo-EM structure determination. *Nat. Methods* **14**, 290-296 (2017).
69. Zivanov, J. *et al.* New tools for automated high-resolution cryo-EM structure determination in RELION-3. *Elife* **7**, 10.7554/eLife.42166 (2018).
70. Kimanius, D., Forsberg, B. O., Scheres, S. H. & Lindahl, E. Accelerated cryo-EM structure determination with parallelisation using GPUs in RELION-2. *Elife* **5**, 10.7554/eLife.18722 (2016).
71. Punjani, A., Zhang, H. & Fleet, D. J. Non-uniform refinement: adaptive regularization improves single-particle cryo-EM reconstruction. *Nat. Methods* **17**, 1214-1221 (2020).
72. Zivanov, J., Nakane, T. & Scheres, S. H. W. A Bayesian approach to beam-induced motion correction in cryo-EM single-particle analysis. *IUCrJ* **6**, 5-17 (2019).

73. Chen, S. *et al.* High-resolution noise substitution to measure overfitting and validate resolution in 3D structure determination by single particle electron cryomicroscopy. *Ultramicroscopy* **135**, 24-35 (2013).
74. Pettersen, E. F. *et al.* UCSF Chimera--a visualization system for exploratory research and analysis. *J. Comput. Chem.* **25**, 1605-1612 (2004).
75. Frenz, B. *et al.* Automatically Fixing Errors in Glycoprotein Structures with Rosetta. *Structure* **27**, 134-139.e3 (2019).
76. Wang, R. Y. *et al.* Automated structure refinement of macromolecular assemblies from cryo-EM maps using Rosetta. *Elife* **5**, 10.7554/eLife.17219 (2016).
77. Liebschner, D. *et al.* Macromolecular structure determination using X-rays, neutrons and electrons: recent developments in Phenix. *Acta Crystallogr. D. Struct. Biol.* **75**, 861-877 (2019).
78. Chen, V. B. *et al.* MolProbity: all-atom structure validation for macromolecular crystallography. *Acta Crystallogr. D Biol. Crystallogr.* **66**, 12-21 (2010).
79. Agirre, J. *et al.* Privateer: software for the conformational validation of carbohydrate structures. *Nat. Struct. Mol. Biol.* **22**, 833-834 (2015).
80. Goddard, T. D. *et al.* UCSF ChimeraX: Meeting modern challenges in visualization and analysis. *Protein Sci.* **27**, 14-25 (2018).